Rheology and Flow Behavior of Starch Nanoparticle Dispersion

by

Yifan Wu

A thesis
presented to the University of Waterloo
in fulfillment of the
thesis requirement for the degree of
Master of Applied Science
in
Chemical Engineering

Waterloo, Ontario, Canada, 2017

AUTHOR'S DECLARATION

I hereby declare that I am the sole author of this thesis. This is a true copy of the thesis, including any required final revisions, as accepted by my examiners.

I understand that my thesis may be made electronically available to the public.

Abstract

With the extensive awareness of environment friendly around the world, more and more researchers are currently developing and modifying bio-based materials that have various potential applications in different fields, such as packaging, paper coating, pharmaceutical industry and so on. Ecological concerns are the main reasons behind this renewed interest in natural and compostable materials. Starch nanoparticles are one of the most potential material not only because they are renewable, biocompatible, and biodegradable with the perspective of sustainable development, but also because of their unique properties at the nanoscale. However, few scholars systematically examined the basic physical properties, rheology and flow behavior of starch nanoparticles, which inspires us to explore this topic.

In order to gain the general knowledge of starch, the structure of starch, category of starch nanoparticles and application of starch nanoparticles were presented in the background chapter. Then the experimental work was mainly consisted of two sections: bench-scale experiments and pilot-scale experiments. The properties of starch nanoparticles, such as swelling property, aging effect, surface tension, conductivity and shear viscosity, were measured in bench-scale experiments, and the pipe behavior of starch nanoparticles dispersion was analyzed in pilot-scale experiments.

To summarize the results, it is found that the size distribution of starch nanoparticles dispersion shifts toward larger number with increasing the mass fraction. Moreover, the shelf life of prepared starch nanoparticles dispersion is relatively long due to there is no aging effect on the size distribution of dilute dispersion and shear rate of concentrated dispersion. The pH and salt concentration do not affect the swelling property, but the starch nanoparticles disperse faster at high pH situation. In addition, the viscosity of starch suspension decreases with increasing the temperature and increases with increasing the concentration. In the case of surface tension and conductivity, it is observed that the starch nanoparticles can lower the surface tension between water and gas and have a very weak effect on the conductivity. Finally, the pumping behavior of starch nanoparticles dispersion is not significantly different from water, in other word, there is no drag reduction effect of starch nanoparticles.

Acknowledgements

First and foremost, I would like to thank my advisor Professor Rajinder Pal for the continuous support of my master study and related research, for his patience, motivation, and immense knowledge. His guidance helped me in all the time of research and writing of this thesis.

I would also like to thank the Prof. Juewen Liu who provided the Malvern Zetasizer to measure the particle distribution, the technical staff Bert Habicher who fixed the broken equipment, the graduated master Jia Yang who taught me how to run the flow loop experiment and the co-op student Michael Shon who helped me to finish the viscosity and pipe behavior measurement. Without their professional participation and input, the research could not have been successfully conducted.

Finally, I must express my very profound gratitude to my parents for providing me with unfailing support and continuous encouragement throughout my years of study and through the process of researching and writing this thesis. This accomplishment would not have been possible without them. Thank you.

Table of Contents

List of Figures

List of Tables

Chapter 1
Background

1.1 Starch

Starch, the most common dietary source of carbohydrates, is a natural, renewable, affordable, and biodegradable polymer consisting of a large number of glucose units joined by glycosidic bonds. It is the most abundant storage polysaccharide in plants, and usually found in plant roots, stalks, crop seeds, and staple crops such as rice, maize, wheat, tapioca and potato[1,2].Worldwide the main sources of starch are corn (82%), wheat (8%), potatoes (5%), and cassava (5%) from which tapioca starch is derived[3].

Wet grinding, sieving and drying is the most common starch industry extraction and refinement process for commercial starch production. Starch is either used as directly extricated from the plant and is called "native starch", or it experiences at least one chemical modifications to reach specific properties and thus is "modified starch", aka "starch alternatives"[4]. In 2008, the world starch market was estimated to be 66 million tons, including nature starch and alternatives. The value of the sales is worth $51.2 billion in 2012,[5] explaining the industrialists and researchers seeking new properties or high value application.

After extraction from plants, starch occurs as a flour-like white powder called starch granules, which from various botanic origin differ in size, ranging from 2 to 150 microns. Their shape may be aspheric or polygonal depend on their botanic resource,[4] as seen in the photomicrographs of corn, wheat, and waxy maize in Figure 1-1, Figure 1-2 and Figure 1-3.

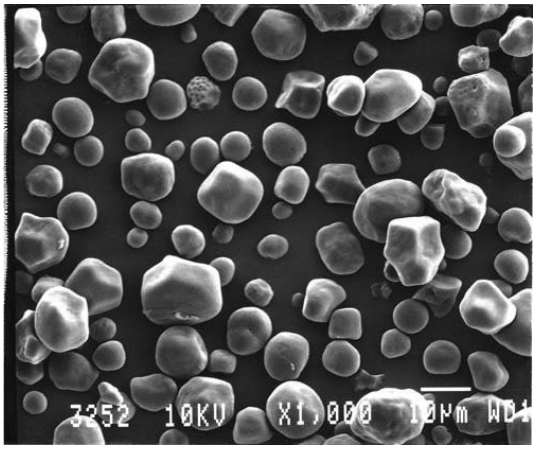

Figure 1-1 SEM of normal corn starch granules (1000X).[4]

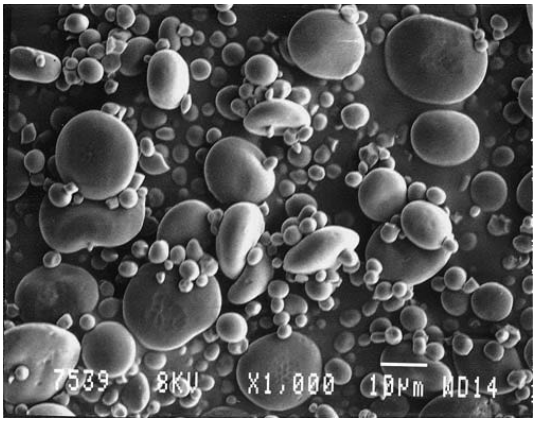

Figure 1-2 SEM of wheat starch granules (1000X).[4]

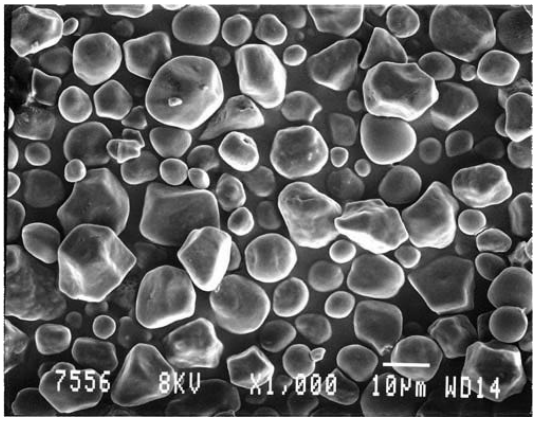

Figure 1-3 SEM of waxy maize starch granules (1000X).[4]

1.1.1 Content

Chemically, starches are polysaccharides, composed of a number of monosaccharides or sugar (glucose) molecules linked together with α-D-(1-4) and/or α-D-(1-6) linkages.

Starch's composition was first determined by studying the residue of its total acid hydrolysis. It is made up of two kinds of molecules, a linear fraction, amylose, and its branched counter-part, amylopectin, whose parts are connected by glycosidic linkages. In most general kinds of cereal endosperm starches, the relative weight percentages of amylopectin range from 72% to 82%, and relative weight percentages of amylose range from 18% to 33%. However, these data sometimes are hugely affected by genotypes, for instance some mutant genotypes of maize (Zea mays) contain as much as 70% amylose whereas other genotypes, called waxy, contain less than 1% amylose.

Amylose molecules typically make up approximately one-quarter of starch. As showed in Figure 1-4, amylose is a long linear chain composed of thousands of glucose units with attachment of the carbon 1 and carbon 4 of glucose units, and therefore contains α-D-(1-4) glycosidic linkages. It forms a three-dimensional network when molecules associate upon cooling, and is responsible for the gelation of cooked, cooled starch pastes.

As major component of starch, amylopectin molecules that is highly branched and bushy, showed in Figure 1-5, constitute approximately three quarters of the polymers in a starch granule. The glucose chain of amylopectin contains α-D-(1-4) linkages, similar to amylose; however, with α-D-(1-6) branching at every 15–30 glucose units of the chain. There is a linkage between the carbon 1 of the glucose and carbon 6 of the branch.

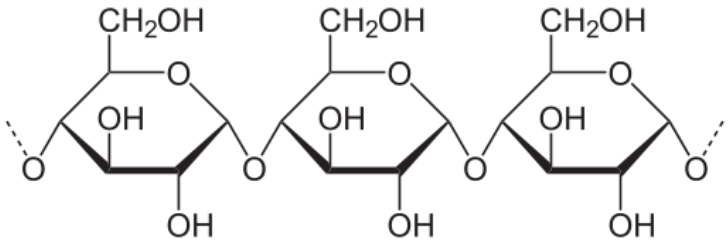

Figure 1-4 Amylose.

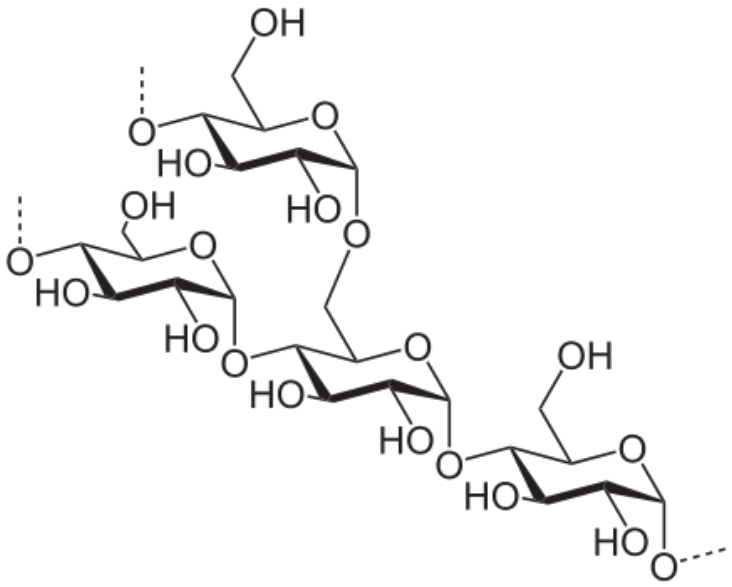

Figure 1-5 Amylopectin.

1.1.2 Structure

Starch structure has been under examination for decades, but a universally accepted model has been lacking since its complexity.[6] However, a predominant model seems to have developed in this past decade. It consists in a multiscale structure as presented in Figure 1-6. The granule (a, 2–100 μm) consists in alternating amorphous and semi-crystalline growth rings (b, 120–400 nm[7]), rendering an onion-like structure when observed under a scanning electron microscope. These growth rings consist respectively of small and larger blocklets (d, 10–100 nm) made of alternating crystalline and amorphous lamellae (c, 9 nm[8]) containing (g) amylopectin, and (h) amylose chains (0.1–1 nm).

Pores can be observed on the surface of starch granules as seen in Figure 1-6a. They are believed to be amorphous channels, as shown in Figure 1-7b, going through the growth rings to the center of the granule (called hilum). Observed under a microscope and polarized light, starch shows birefringence. Indeed, starch granules consist of concentric alternating amorphous and semi-crystalline growth rings growing by apposition from the hilum. The shape and particle size of granules, as well as the number and thickness of the growth rings, is strongly dependent on botanic origin.

There are two hypotheses, blocket concept and fibrillary concept, were developed in the history of researching the internal structure of granules. But blocket concept gradually is accepted because more and more evidences including SEM and AFM images support this concept.[9]

According to blocket concept, both semi-crystalline and amorphous growth rings are subdivided into respectively large (~100nm) and small (~25nm) ellipsoid blockets.[8] And the size of blockets mainly depends on the botanic origin of starch and their location in the granule.

These blocklets are proposed to contain 280 amylopectin side chain clusters based on they have an average size of 100 nm in diameter.[10] Schematically, the semi-crystalline growth rings consist of a stack of repeated crystalline and amorphous lamellae (depicted in Figure 1-6c and Figure 1-7c). The thickness of the combined layers is 8-9 nm regardless of the botanic origin.[8]

The crystalline lamellae are believed to be created by the intertwining of amylopectin side chains with a linear length above 10 glucose units to form double helices.[11] These double helices are packed together to form the crystallites. The amorphous regions correspond to branching points of amylopectin.

Depending on their X-ray diffraction (XRD) pattern, starches are categorized in three crystalline types called A, B, and C. Imberty et al.[12,13] proposed a model for the double helices packing configuration to explain the difference between A and B types starches. A-type structures are closely packed with water molecules between each double helical structure, whereas B-types are more open and water molecules are located in the central cavity formed by six double helices as shown in Figure 1-7e. C-type starch pattern has been considered to be a mixture of both A- and B-types since its XRD pattern can be resolved as a combination of the previous two.

Individual amylose chains are believed to be randomly located in a radial fashion in both the crystalline and the amorphous regions.[11] The concentration of amylose (and lipid) increases towards the surface of the granule, with smaller amylose chains predominating near the surface. Amylose chains are believed to be in a single helical state, although a small proportion may be involved in lipid complexes. Some of the larger amylose chains may be involved in double helical interactions with amylopectin.[9]

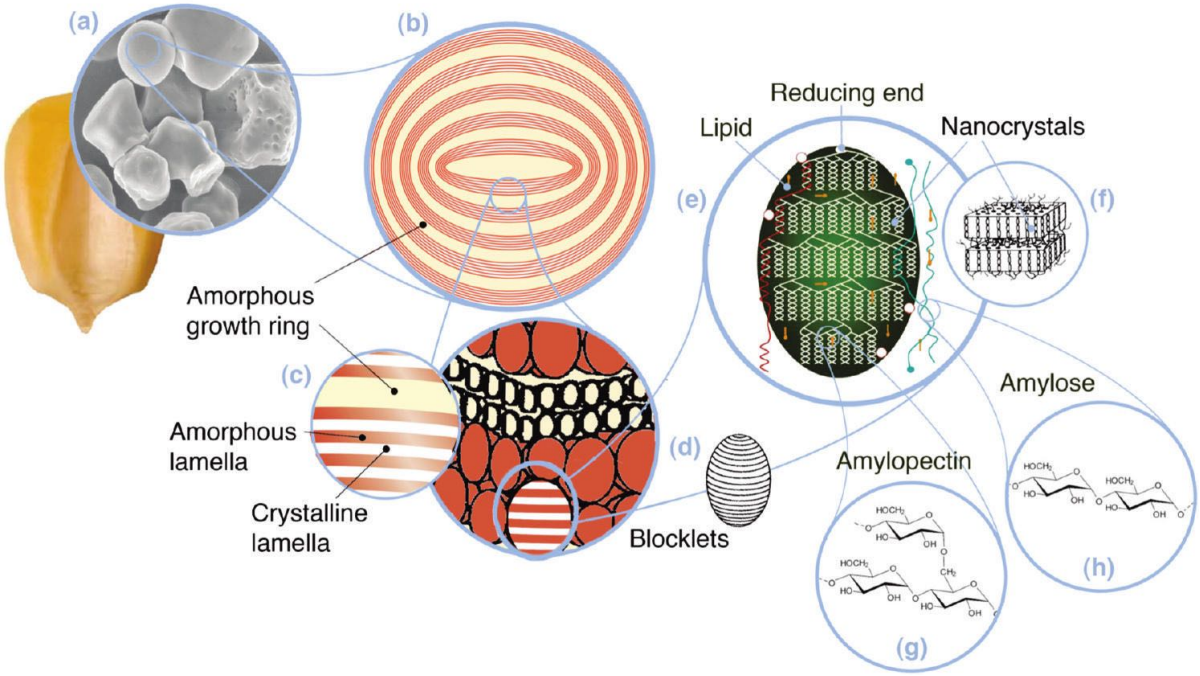

Figure 1-6 Starch multiscale structure. (a) Starch granules from normal maize (30 µm); (b) amorphous and semi-crystalline growth rings (120–500 nm); (c) amorphous and crystalline lamellae (9 nm): magnified details of the semi-crystalline growth ring; (d) blocklets (20–50 nm): constituting unit of the growth rings; (e) amylopectin double helices forming the crystalline lamellae of the blocklets; (f) nanocrystals: other representation of the crystalline lamellae called SNC when separated by acid hydrolysis; (g) amylopectin's molecular structure; (h) amylose's molecular structure (0.1–1 nm).[1]

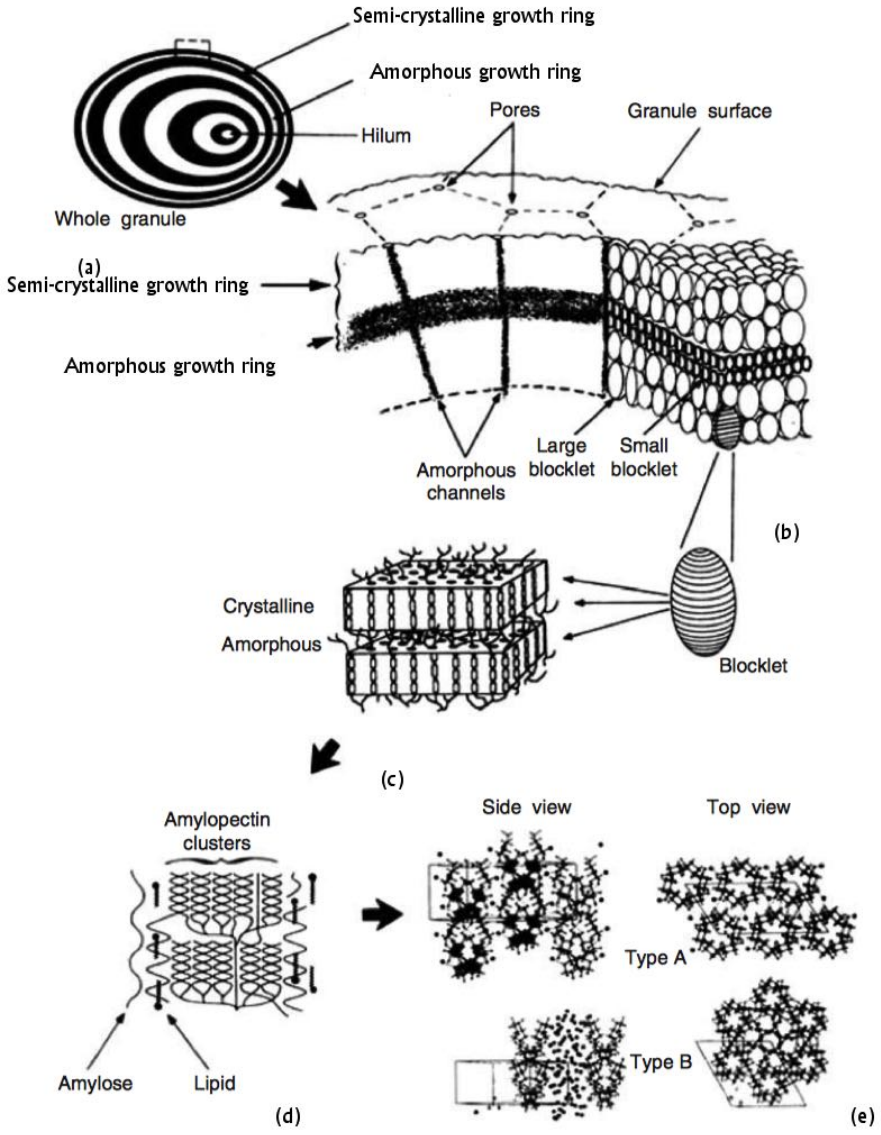

Figure 1-7 Overview of starch granule structure. (a) Semi-crystalline growth ring and amorphous growth ring. Rings are thinner towards the granule exterior (due to increasing surface area to be added to by constant growth rate) and the hilum is shown off-center; (b) The blocklets structure is shown in association with amorphous radial channels. Blocklet size is smaller in the amorphous growth rings than in the semi-crystalline growth rings; (c) One semi-crystalline blocklet is shown containing several amorphous and crystalline lamellae; (d) amylopectin is shown in the lamellae; (e) Double helixes packing configuration according to crystalline type.[9]

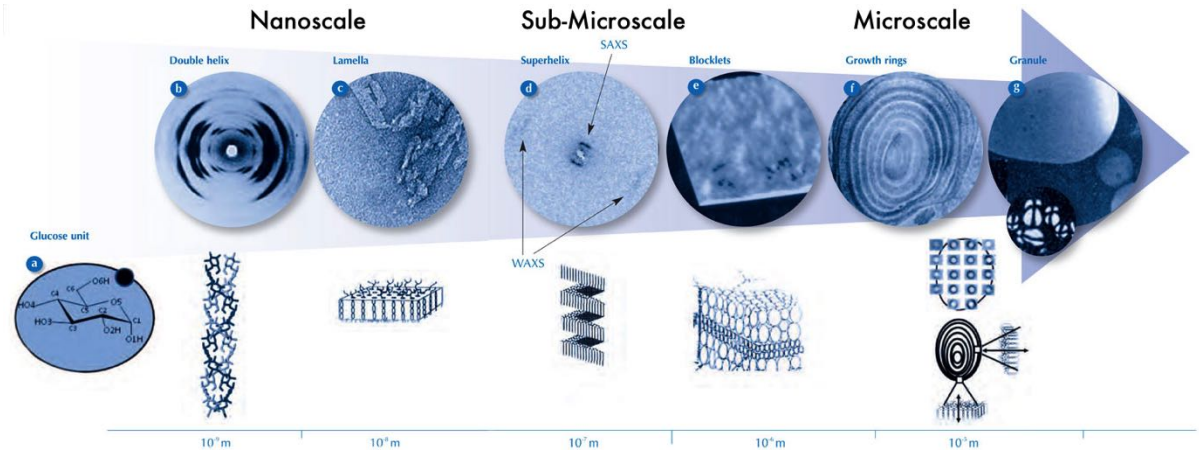

Figure 1-8 The levels of starch organization: (a) Glucose unit; (b) Double helix; (c) Lamella, bottom is a model of a crystalline lamella made of about 100 double helices; (d) Superhelix: bottom is the superhelix model, with a pitch of 9 nm and a diameter of 18 nm; (e) Blocklets: bottom is blocklet model. The blocklets are believed to be smaller in the amorphous regions (central region) than in the semi-crystalline regions (above and below); (f) Growth rings; (g) Granule.[14]

In summary, the complexity and heterogeneity of starch granule are described by a multiscale model. Three main levels of hierarchical organization, shown in Figure 1-8, which have been discussed in this chapter: (1) the microscale level: several micrometers to hundred micrometers depending on the botanic origin, consisting of onion-like growth rings; (2) the ultrastructure at an observation scale of several hundred nanometers, comprising the material building up both amorphous and semi-crystalline growth rings. Blockets can be distinguished; (3) the nanoscale: amorphous lamella and crystalline lamella can be distinguished at an observation scale of several nanometers, which consist the double helix.

1.2 Starch nanoparticles

1.2.1 Preparation

Starch nanoparticles (SNP) can schematically be divided into two categories according to which property of starch is used: (1) those exploiting the semi-crystalline property of starch, such as starch nanocrystals (SNC); and (2) those exploiting the gelatinizing/melting property of starch referred to as regenerated or colloidal SNP. They can further be classified by their production protocol as showed in

Figure 1-9. SNC are mainly prepared by hydrolysis including acid or enzymatic hydrolysis, gamma radiation[15] or regeneration using cocrystallization[16], while regenerated or colloidal SNP are prepared by regeneration using cross-linking[17,18], mechanical treatment using extrusion[19,20] or microfluidizers[21].

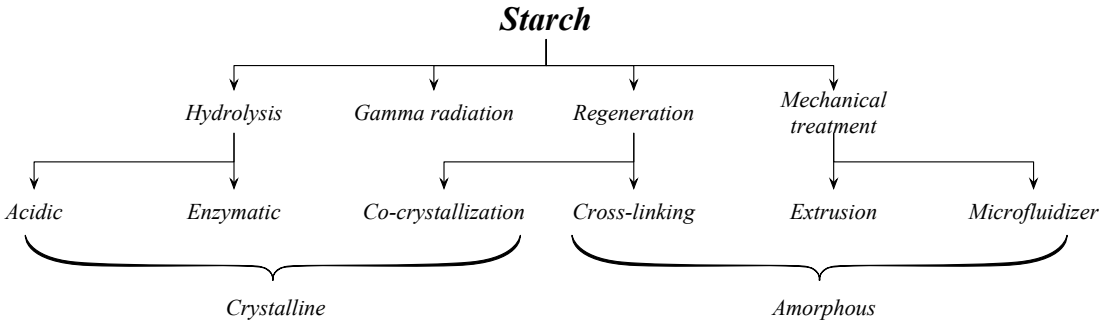

Figure 1-9 Different ways of producing crystalline and amorphous starch nanoparticles: hydrolysis leads to nanocrystals, whereas regeneration and mechanical treatment lead to both amorphous and crystalline particles.[22]

1.2.1.1 Crystalline starch nanoparticles

First of all, it is important to clarify the terms commonly used. Starch crystallite, starch nanocrystal, microcrystalline starch, and hydrolyzed starch all refer to the crystalline part of starch obtained by hydrolysis but to a different extent (from the most to the least). It has to be distinguished from amorphous starch nanoparticles, presented later.

Hydrolysis, a chemical process in which a molecule of water is added to a substance, has been used for a long time to modify starch and its properties. Acid hydrolysis is the most popular method and its mechanical has been researched for decades.

For all starches a two-stage hydrolysis profile can be evidenced: (1) an initial fast hydrolysis step, presumably due to the hydrolysis of the amorphous regions of starch granules, and (2) a second slower step, presumably due to the hydrolysis of the crystalline regions[23,24]. Some authors distinguish three steps of hydrolysis: a rapid one, a slow one, and a very slow one[25], presumably corresponding to the hydrolysis of amorphous layers, semi-crystalline layers, and crystalline ones, respectively.

The hydrolysis preparation protocol is straightforward. Generally, a given amount of starch granules is mixed with a given volume of acid including HCl and H_2SO_4 in a container and stirred constantly at specific revolutions per minute (rpm) while maintained at optimized temperature. After 5 days, the suspension is washed by successive centrifugations with distilled water until neutrality. Then the crystalline starch nanoparticles are prepared.

The obvious factors influencing hydrolysis kinetic are: time, acid type, acid concentration, and temperature. And the difference in the rate and yield of hydrolysis among starch types was attributed to the difference in granule sizes and number of pores on the granule surface[26]. However, Biliaderis and Grant[23] thought that the granular organization had probably more influence. They concluded that (1) the first stage of hydrolysis (amorphous regions) is influenced by the granule size, pores on the surface, amylose content, and the amount of lipid-complexed amylose chains, and (2) the second step of hydrolysis (crystalline region) is influenced by the amylopectin content, mode of distribution of α-D-(1-6) branches between the amorphous and the crystalline regions, and degree of packing of the double helices within the crystallites (i.e., the parameters also influencing crystallinity).

To our knowledge, no work on a purely enzymatic hydrolysis method for producing SNC has been developed. However, an attempt to produce starch nanocrystals by enzymatic hydrolysis were reported by Kim et al.[27], it is believed that the process leads to 500nm blocklets rather than nanoparticles.

Kim and Lim[16] report the preparation of nanocrystals by co-crystallization method, specifically complex formation between amylose and n-butanol. Enzymatic hydrolysis is used to selectively keep crystalline particles.

Despite differences in hydrolysis mechanisms, both enzymatic and acidic hydrolysis studies showed evidence of concentric “soft” layers which are more readily hydrolyzed. Although the origin and structure of the soft layer led to several debates in the 1960s, it was later accepted that it is always the less organized structure that degrades first[28] (corresponding to amylose), leaving more resistant amylopectin-based crystallites.

Gamma radiation, namely gamma ray, is another methodology to produce crystalline starch nanoparticles reported by Lamanna et al.[15] Gamma radiation may generate free radicals on starch molecules which are capable of hydrolyzing chemical bonds, thereby cleaving large molecules of starch into smaller fragments of dextrin. This mechanism was similar to that of the starch acid hydrolysis, that is gamma radiation cleaves the amorphous regions, instead of crystallite regions. It is important to

mention that although free radicals could be involved in the mechanism they easily recombine in water, thus solutions obtained from gamma irradiated samples are radical free.

In summary, the hydrolysis and gamma radiation methodology consist basically in removing starch amorphous regions, yielding crystalline starch nanoparticles.

1.2.1.2 Amorphous starch nanoparticles

Amorphous starch nanoparticles consist of regenerated nanoparticles and nanocolloids. Regenerated nanoparticles are obtained by regeneration-precipitation[3,16,18,29] or by reactive extrusion[20], where cross-linking agents are added to stabilize the nanoparticle structure[30–32], and nanocolloids are formed by microfluidization[21,33]. And gelatinization plays a core role in the process of producing amorphous starch nanoparticles.

In gelatinization, when native starch granules are heated in water, their semi-crystalline nature architecture is gradually disrupted, resulting in the phase transition from an ordered granular structure into a disordered state in water[34,35]. Olkku and Rha[36] summarized the steps of gelatinization, an irreversible process, as follows: (1) granules hydrate and swell to several times their original size, (2) granules lose their birefringence, (3) the clarity of the mixture increases, (4) rapid increase in consistency occurs and reaches a maximum, (5) linear molecules dissolve and diffuse from ruptured granules, and (6) the uniformly dispersed matrix forms a gel or paste-like mass.

In more details, Ma et al.[18] used ethanol as a precipitant to precipitate pre-cooked native starch. Corn starch was mixed with distilled water and completely gelatinized (90°C, 1 hour). Then ethanol was added dropwise to the solution at room temperature and constantly stirred for 50 minutes. The suspensions were centrifuged with ethanol to remove water and the settled material was dried at 50°C to remove ethanol, and SNPs at 50–100 nm were obtained.

Extrusion is an energy efficient system able to break down the starch granule structure through a combination of high shear, temperature and pressure and can successfully melt starch. Typical single or double screw extruders, in general form consists of a hopper, barrel, feed screw, thermocouples, and dies.

SNP prepared via reactive extrusion was reported by Song et al.[20]. The influence of extrusion conditions (such as temperature, screw speed, torque, the content proportion of starch and water) and

cross-linker addition on particle size were systematically investigated. Summarily, native starch granules were premixed with plasticizers (typically water and/or glycerol) and fed into a co-rotating twin-screw extruder. A cross-linker was added in a downstream hopper of the extruder. The extrusion was conducted under a given temperature to allow for starch fragmentation, melting and cross-linking (initiation and curing) reaction. It was found that the addition of cross-linker during extrusion led to a higher torque and reduced particle size (from 300 nm to 160 nm). In this condition, an increase in reaction temperature and/or screw speed (i.e., strain) also strongly contributed to reducing particle size and even size distribution (for temperature). As expected, resulting nanoparticles were almost amorphous due to extrusion, and suspension viscosity was much lower than for gelatinized starch.

Liu et al.[21] applied the method of microfluidization to the production of starch colloids. A 5% slurry of high amylose corn starch was run through a microfluidizer under a given constant high-pressure for several passes (up to 30). The particles size of samples obtained from more than 10 passes was below 100 nm, and the starch slurry changed from sol into gel. The gel-like suspension remained stable for more than a month when diluted to a concentration of 0.5 wt%. The thermal stability was not affected, and since no chemical or thermal degradation occurred during the treatment, the reported yield was almost 100%. However, the resultant starch colloids were obtained from breaking down both amorphous and crystalline domains, rendering an amorphous diffraction pattern after 10 passes.

1.3 Application of starch nanoparticles

Starch nanoparticles are attracting attention from not only the academic field but also industry since it is a renewable, biocompatible and biodegradable nanoparticle. SNP have numerous advantages over conventional inorganic particles such as low density, nontoxicity, biodegradability, biocompatibility, easy surface modification, and functionalization.

1.3.1 Food industry

Nanotechnology has potential applications in all aspects of the food industry, including storage, quality monitoring, food processing, and food packaging. Nanotechnology applications in the food industry range from intelligent packaging to creation of on-demand interactive food that allows consumers to modify food, depending on tastes and nutritional needs.

Packaging plays a variety of important roles in the food industry. The major role of packaging is to protect food from spoilage by microbial contamination, physical damage, or biochemical reactions. Packaging also provides ease in handling, storage efficiency, attractiveness, and product information for food.

Starch-clay are one of the most promising biodegradable nanocomposites candidate for food packaging[37–39]. Novel biodegradable starch/clay nanocomposite films prepared by homogeneously dispersing Montmorillonite nanoparticles via polymer melt processing techniques were reported by Maurizio et al.[40] and a reinforcing effect of the clay particles on the modulus and the tensile strength of the starch was observed.

In order to help food preservation, several researches have considered the use of many additives or food components into biodegradable starch films as a way of improving food shelf life. For instance, García et al.[41] observed that starch-based coatings extended the storage life of strawberries and retarded the senescence process. The effect on water vapor permeability (WVP) and mechanical properties of an addition of various amounts of an acetylated monoglyceride (Acetem) to native potato starch (NPS) films was studied by Petersson and Stading[42].

1.3.2 Pharmaceutical industry

Studies with biodegradable starch-based polymers have recently demonstrated that these materials have a range of properties that make them suitable for use in several biomedical applications, ranging from bone plates and screws to drug delivery carriers and tissue engineering scaffolds[22].

Biocompatible and biodegradable drug delivery systems can preferably be made of naturally occurring polymers such as chitosan, gelatin, polysaccharides, and silk fibroin. The major limitation of current anticancer drugs is their toxicity and lack of specificity.[43] In an attempt to overcome these problems, Bajpai et al.[43] synthesized and characterized cisplatin containing iron oxide-impregnated starch nanoparticles as a possible and potential drug carrier for magnetically mediated targeted drug delivery.

Iron oxide-impregnated starch nanoparticles were prepared by the emulsion cross-linking method, which effectively delivers the antitumor drug cisplatin in the presence and absence of magnetic field via a diffusion-controlled pathway.

In addition, the biomedical industry has shown a great interest in the development of starch nanocomposites for their use as sensors or stimulators of bone cells.[44]

1.3.3 Agricultural Applications

The world consumption of plastic materials in agriculture amounts yearly to 6.5 million tons, used to improve crop cultivation and protect agricultural products after harvesting, in the form of greenhouses, tunnels, mulch, silage films, and bale wraps. Therefore, there is a huge amount of plastics discarded into the environment, buried in the soil, or burnt by farmers, releasing harmful substances with the associated negative consequences to the environment. A solution to this problem can be the introduction in agriculture of biodegradable films, which can be disposed directly into the soil or into a composting system at the end of their lifetime.

Therefore, starch nanoparticles look like a good alternative for developing starch-based nanocomposites with high transparency. This was reported in the study of Gonçalves et al.[45], with nanocrystals obtained from the seeds of pinhão (Araucaria angustifolia). The greater solubility and reduced turbidity are interesting from a commercial standpoint, indicating that pinhão starch nanoparticles could be useful for development of coating materials or films composites.

Taking into the account the serious problems that have been caused by mistreatment ecology due to the increasing use of synthetic materials, necessary awareness must be given to the replacement of these treacherous by materials that are friendly to both the environment and human health. Furthermore, the increasing use of synthetic polymers or plastics as a result of the growing human population and standard of living will result in higher demands on oil production and will contribute to a possible depletion of crude oil before the end of the century. The implement of the bio-based polymers that are produced from renewable resources will offer important contributions by reducing the dependence on fossil fuels and through the related positive environmental impacts such as reduced carbon dioxide emissions.

Chapter 2
Materials and Methods

2.1 Materials

Experimental grade biopolymer starch nanoparticles were provided by EcoSynthetix. Preservation ACTICIDE® GA was provided by THOR Specialties, Inc. Sodium chloride (GR for analysis) was purchased from EMD Chemicals Inc. Sodium hydroxide and hydrochloric acid were obtained from Sigma-Aldrich Co. LLC.

2.2 Preparation of pH-salt solution

There are four kinds of pH-salt solution, pH = 3 & 1mM NaCl, pH = 3 & 100mM NaCl, pH = 11 & 1mM NaCl and pH = 11 & 100mM NaCl, were prepared by adjusting the pH of mixture of distilled water and sodium chloride using NaOH buffer and HCl buffer.

2.3 Preparation of starch dispersion

For dilute dispersion, a mixture of calculated wt% starch nanoparticles and 100ml pH-salt solution containing 0.15wt% preservation was homogenized at 1600 rpm for 90 mins at 21 °C with a laboratory magnetic stirrer (VWR® hotplate stirrers, CORNING® PC-420D stirrer and CORNING® PC-353 stirrer).

Similarly, for middle and high concentration dispersion, a mixture of specific wt% starch nanoparticles and 500 ml distilled water containing 0.15wt% preservation was homogenized at 40-85 volts at 21 °C initial temperature with a tabletop lab homogenizing mixer (GIFFORD WOOD, model 1L). Because of the limitation volume of the mixing container, mixing time depends on the amount of starch powders varied from 20 mins to 60 mins. But the rule of thumb was that mixing 20 mins after all of the starch added in. And the temperature will increase in the whole mixing process due to the friction between dispersion and rotator, the maximum temperature can go to 70 °C.

2.4 Dilute dispersion viscosity measurements

The relative viscosity ($\eta_r = \eta / \eta_o$) was measured by glass CANNON® Ubbelohde dilution viscometer (for the starch dispersion η and for its dispersion medium η_o that is water).

Suspension behaviour in the dilute limit was first addressed theoretically by Einstein, who derived an analytical solution for the hydrodynamics around an isolated sphere which yields[46]:

$$\eta_r = 1 + B\emptyset \tag{2.1}$$

where Φ is the volume fraction and the constant B is variously referred to as the 'Einstein coefficient' or the 'intrinsic viscosity', which indicates the swollenness of particles. Usually the equation takes the value B = 2.5 assuming the particles are rigid and no swelling. Therefore, the swollenness of particles can be interpreted by the constant B that can be obtained from linear regression between relative viscosity and volume fraction. The room temperature was maintained at 21 ºC during the viscosity measurements.

2.5 Rheological measurements

The shear viscosities were measured by a HAAKE viscometer Rotovisco® RV 12 with system MV I (shear rate up to 1198 s^{-1}). The solvent viscosities of starch dispersion were measured at 21 °C.

2.6 Particle size measurement by nanoparticle tracking analysis

Particle size analysis of the dispersed starch nanoparticles was performed using the Zetasizer Nano zs90 manipulated by Malvern Instruments Ltd. And the software edition is Zetasizer software 6.20. All of the size dispersion data were measured in the ZEN0112, low volume disposable sizing cuvette, at default settings, that is experiment temperature was 25 °C, the equilibration time was 120s and delay between different measurements was 5s. The number of measurements varied according to different situation.

2.7 Zeta potential measurements

The zeta potential distribution was performed using Zetasizer Nano zs90 manipulated by Malvern Instruments Ltd. And the software edition is Zetasizer software 6.20.

2.8 Pumping behavior measurements

2.8.1 Experimental set-up

The experiments were performed in a closed loop system. Figure 2-1 shows a schematic diagram of the experimental set-up.

The starch nanoparticles dispersion was prepared in a large mixing tank (Figure 2-2a), which had a jacket and a thermal controller to maintain the required temperature during experiments, with a powerful motor stirrer. Two different capacity centrifugal pumps were used to circulate fluid samples. Three straight tubes (Figure 2-2c) with different diameters (Table 2-1) were installed horizontally. Each tube was equipped with three pressure taps which were made by drilling small holes (1/10 of tube diameter) through the tube walls. The pressure transducers were configured in such a manner that a desired pressure transducer could be easily connected to the pressure taps while they were in use. The pressure taps were located far enough from the tube entrance to ensure that the flow of test fluid was fully developed in the section of the tube where measurements were taken place. The first pressure tap was used as the reference tap for measuring the differential pressure between two taps. The loop has been equipped with a data acquisition system which consisted of an electronic board for input and output signals and a computer terminal (Figure 2-2d) to process signals and gather data using the LABVIEW software.

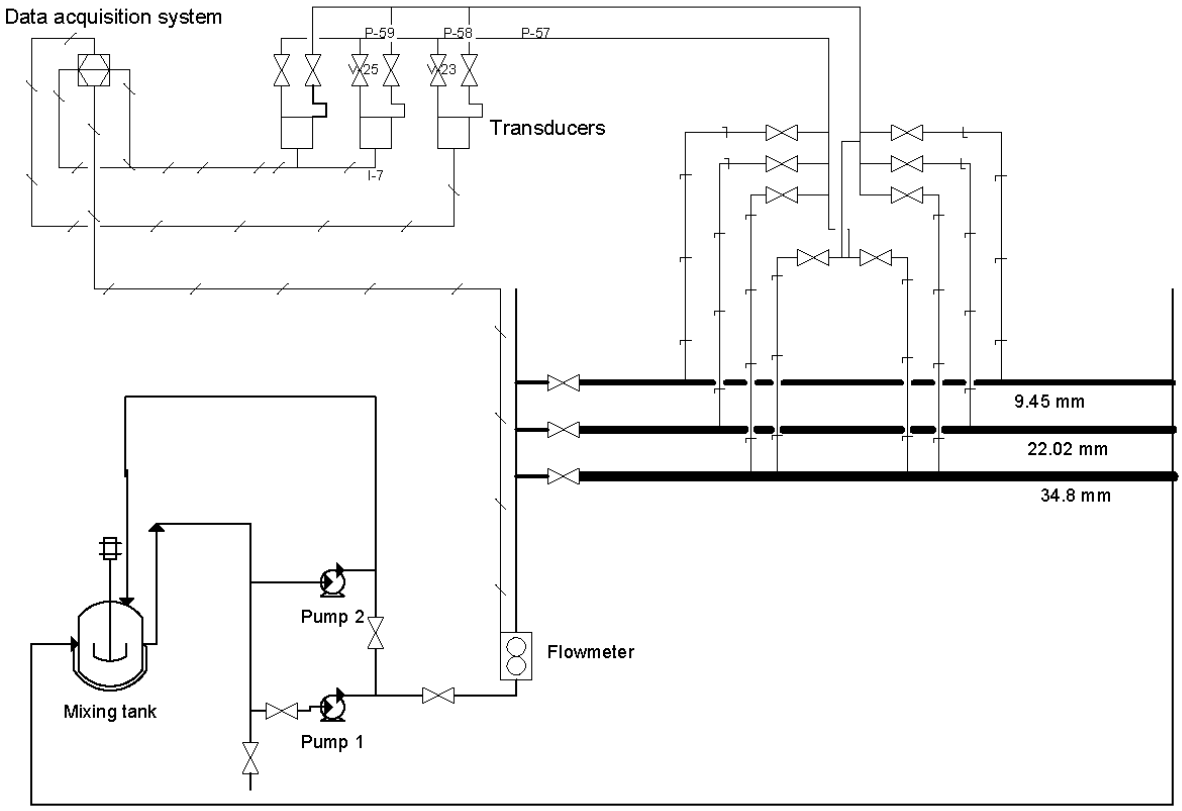

Figure 2-1 Schematic diagram of the experimental setup.[47]

Figure 2-2 Photos of pipeline flow loop set-up: (a) the mixing tank; (b) the control panel; (c) different size pipelines, from top to bottom is 0.5 inch, 1.0 inch and 1.5 inch; (d) the computer terminal of data acquisition system.

Table 2-1 The dimension of tubes and test point locations

Pipe No.	Nominal diameter (inch)	Inside diameter (mm)	Entrance length (cm)	Test section length (m)
1	0.50	9.45	91.44	1.219
2	1.00	22.02	154.20	0.910
3	1.50	34.80	154.20	3.048

2.8.2 Coriolis flowmeter

The flow rate was measured by a KROHNE Coriolis flowmeter embedded in the flow loop system. In order to ensure accurate and reliable measurement data, the flowmeter was calibrated by measuring (weighing) the amount of water passing the flowmeter in a certain time.

The purpose of a meter calibration effort is to ascertain a flow calibration factor that is used to convert electronic signals to direct measurements of flow rate. Coriolis meters are known in the art as linear meters, that is the flow calibration factor is a constant with respect to flow rate, therefore the calibration equation was obtained by linear regression of data points.

Calibration data were plotted in the Figure 2-3, and the linear regression equation is:

$$y = 1.5008\,x - 1.5244 \tag{2.2}$$

where x is the reading voltage, y is the flow rate which unit is kg/s.

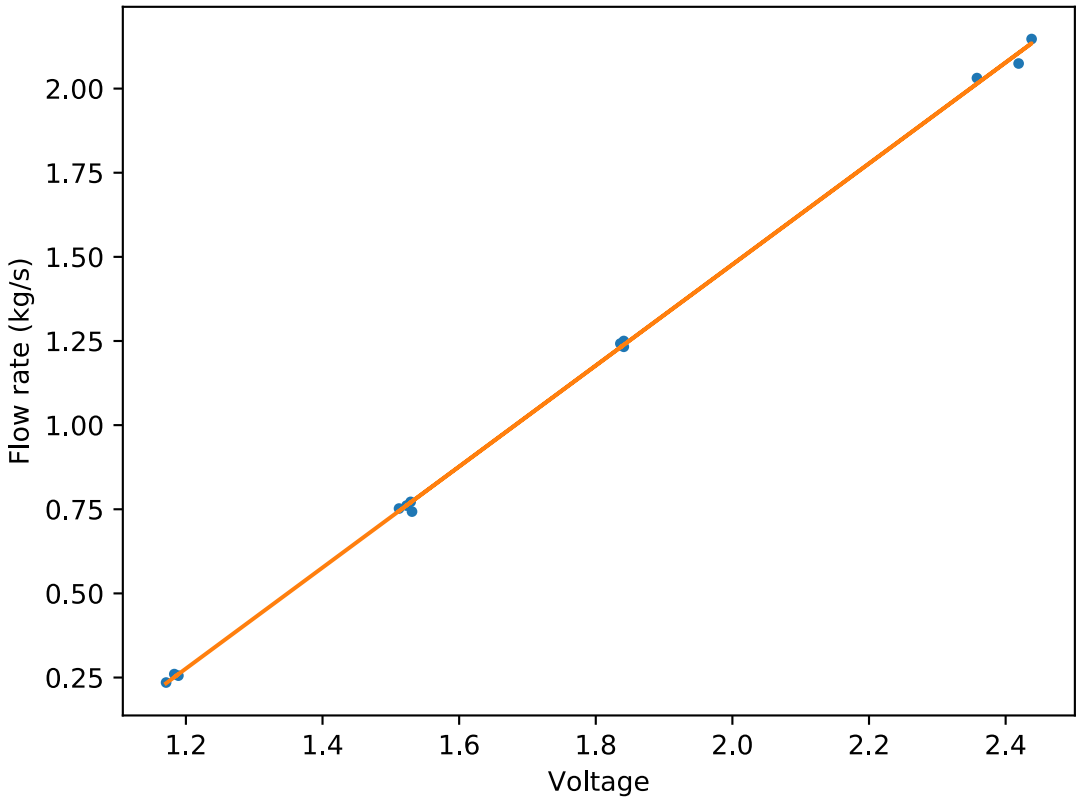

Figure 2-3 Flowmeter calibration.

Other related information regarding the flowmeter is presented in Appendix C.

2.8.3 Pressure transducers

Three independent pressure transducers with different measurement ranges were installed. Every transducer was connected with two shut-off valves and one bypass valve as shown in Figure 2-4.

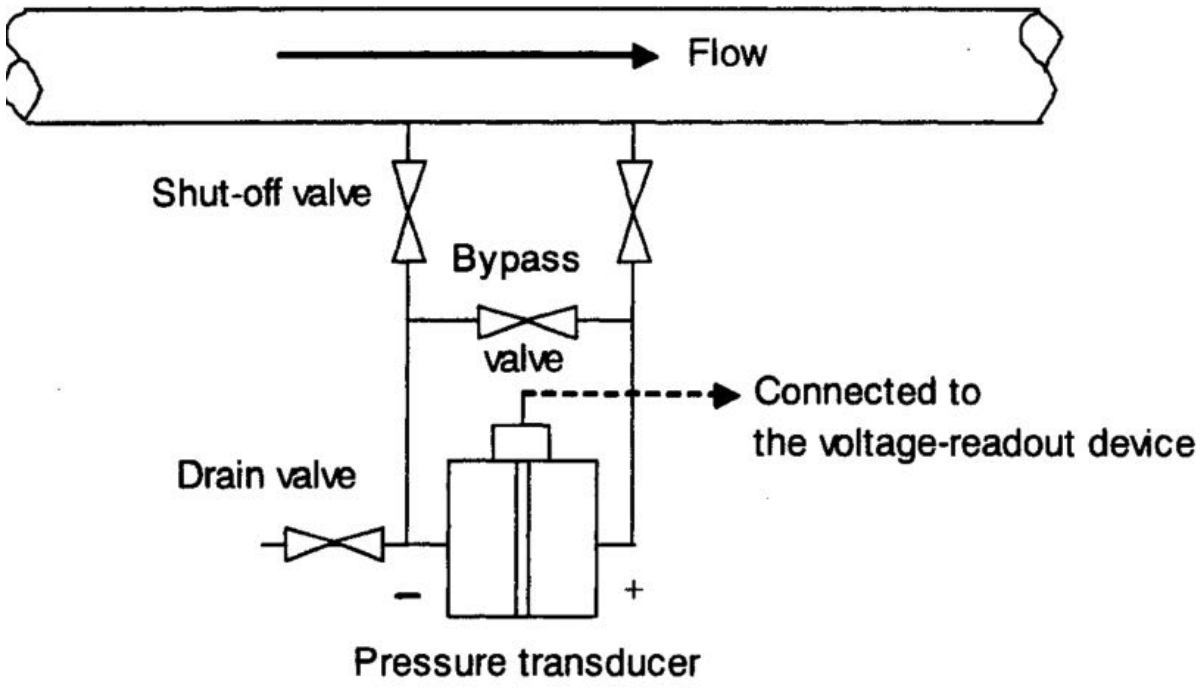

Figure 2-4 Pressure transducer connection diagram.[47]

The pressure transducers were calibrated by Dr. Mohsenipour[47] when the whole loop system was built up. The relative regression equations of different pressure transducers are listed in Table 2-2.

Table 2-2 Pressure transducer calibration equations, where x is reading voltage and y is differential pressure with unit of psi.[47]

Measure Range (psi)	Regression model
0 – 10.0	$y = 2.5297\,x - 2.5573$
0 – 5.0	$y = 1.2581\,x - 1.2823$
0 – 0.5	$y = 0.1221\,x - 0.1020$

Chapter 3
Results and Discussion

3.1 Size distribution of starch nanoparticle dispersion

To understand the nanostructure of starch nanoparticles, the size distributions of starch nanoparticles were examined by dynamic light scattering (DLS) at different concentration. The average particle sizes are given in Table 3-1 and plotted in Figure 3-1. It was found that the relation between starch concentration and average nanoparticle size was not linear. This result is consistent with the correlation reported by Hisfazilah Saari et al.[48].

The size distributions of at different concentration were shown in Figure 3-2 and Figure 3-3. As can be observed from Figure 3-3, increasing the mass fraction of starch nanoparticles from 1.96 wt% to 13.04 wt% could shift the peak of starch nanoparticles sizes distribution from around 20 nm to thousands nanometer. The observed increase in particle size of nanoparticles could be attributed to the nanoparticles partially aggregated at higher starch concentrations[48].

Table 3-1 Mean particle size of starch nanoparticles determined by dynamic light scattering at different concentration.

Mass fraction	Mean diameter (nm)	Standard deviation
1.96%	16.62	5.70
5.49%	124.61	19.11
7.41%	842.96	658.35
13.04%	3129.99	1607.54

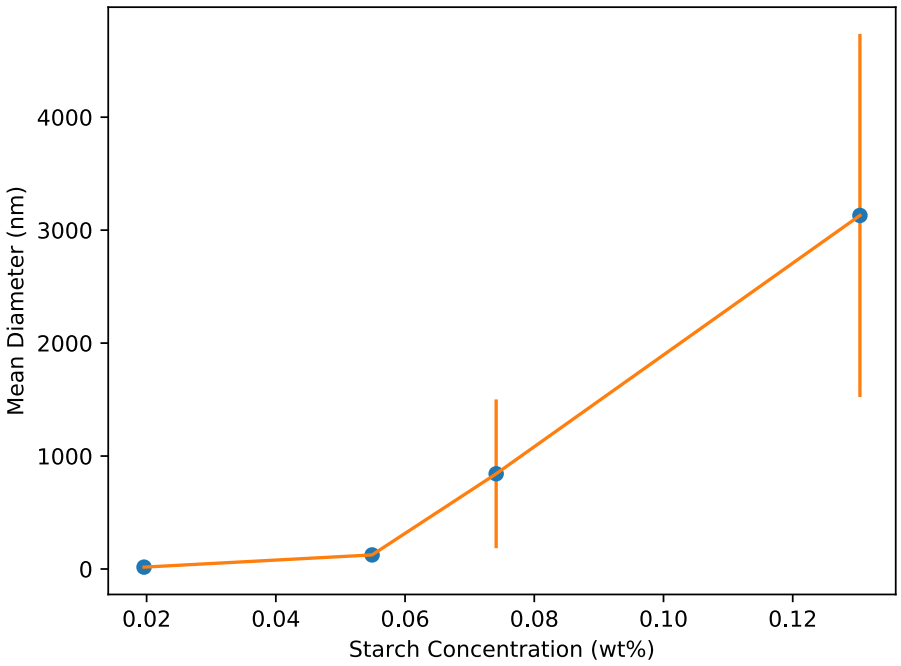

Figure 3-1 Mean particle sizes at different concentration.

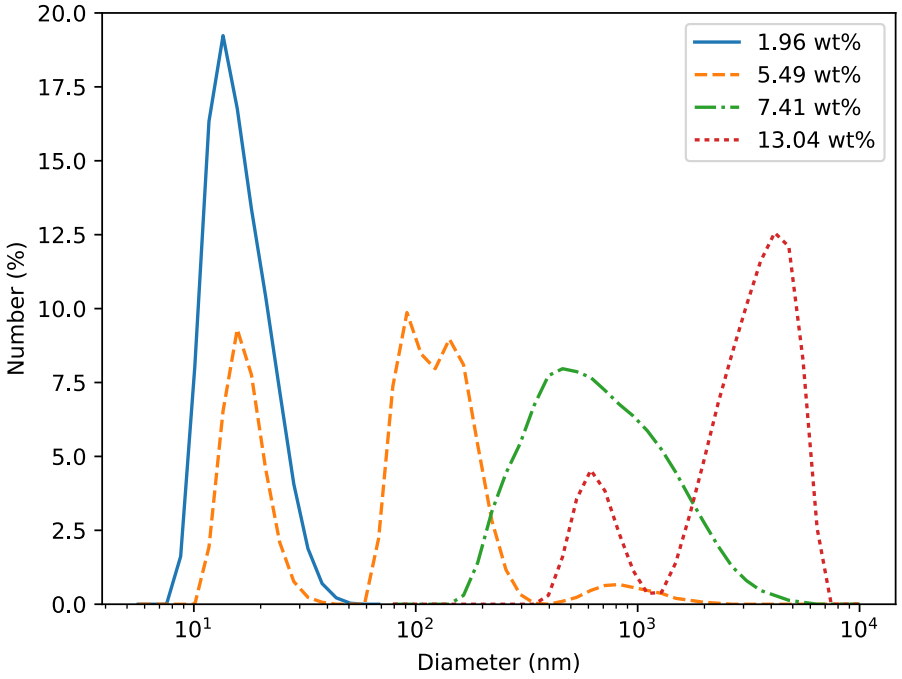

Figure 3-2 Combined size distribution of starch nanoparticles at different concentration: solid line is 1.96 wt%; dashed line is 5.49 wt%; dash-dot line is 7.41 wt%; dotted line is 13.04 wt%.

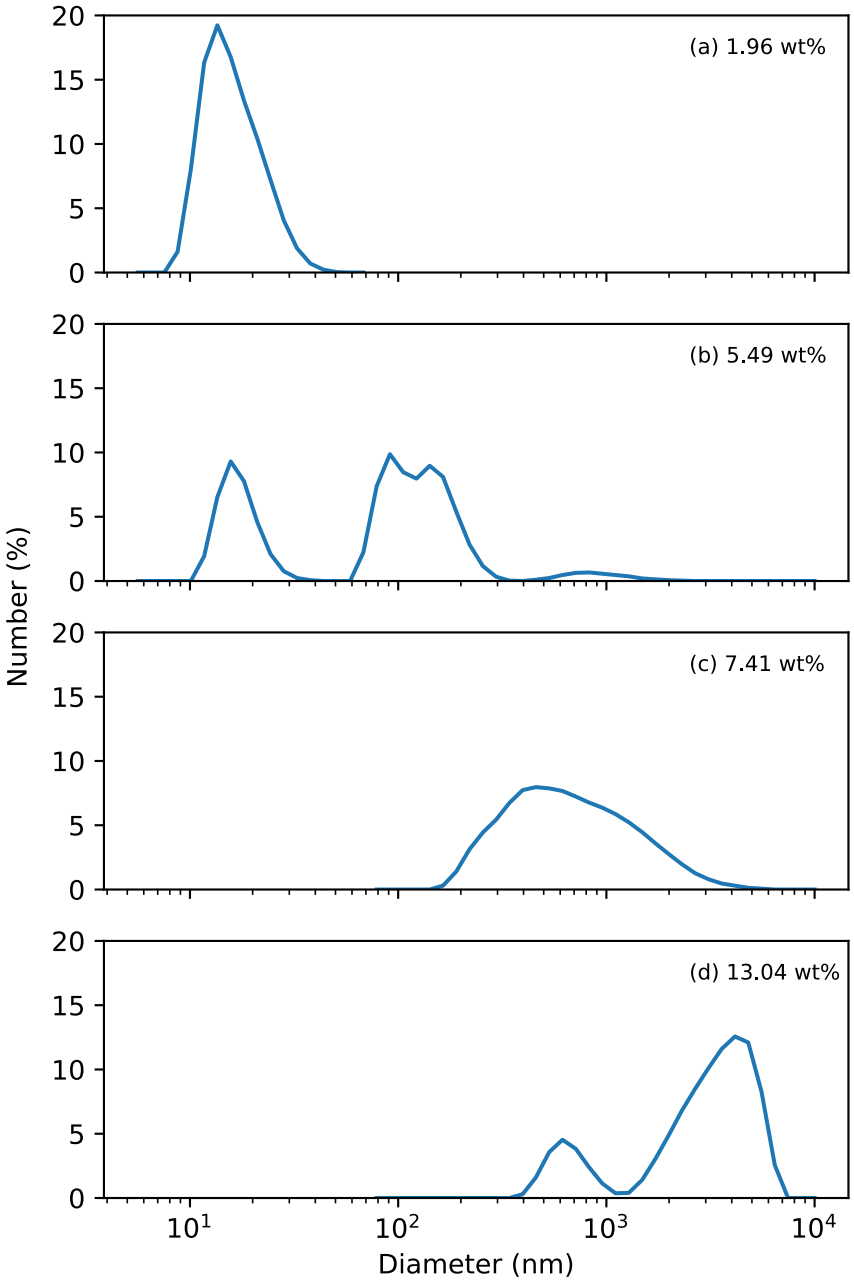

Figure 3-3 Size distribution of starch nanoparticles at different concentration: (a) starch nanoparticles mass fraction is 1.96 wt%; (b) starch nanoparticles mass fraction is 5.49 wt%; (c) starch nanoparticles mass fraction is 7.41 wt%; (d) starch nanoparticles mass fraction is 13.04 wt%.

The above plots naturally raise a question, are these aggregations permanent? If they are, we need to pay much more attention when preparing the dispersion, because the initial concentration will play a critical role in the microcosmic morphology of starch nanoparticles. On the contrary, if the aggregations were temporary, there will be a lot of flexibility for the future experiments and applications. For instance, high concentration starch nanoparticle dispersion can be diluted and used as low concentration dispersion without effecting the nanostructure.

In order to ascertain whether the aggregations of the nanoparticles are permanent or not, an additional experiment was used to investigate changes in size distribution of diluted low concentration dispersion and normal one. The size distribution of 30 wt% dispersion went out of the range of the DLS equipment, then the dispersion was diluted to 2.28 wt% solution by manually homogenizing in the specific amount of de-ionized water with glass stirrer. As the results shown in Figure 3-4, the result of diluted starch nanoparticles dispersion is almost identical with its counterpart.

As a result of the above analysis, it was found that the size distribution of starch nanoparticles shift increases with increasing concentration. Although aggregations spontaneously form at middle or high concentration dispersion, they are temporary and can be induced by diluting high concentration dispersion into low concentration one.

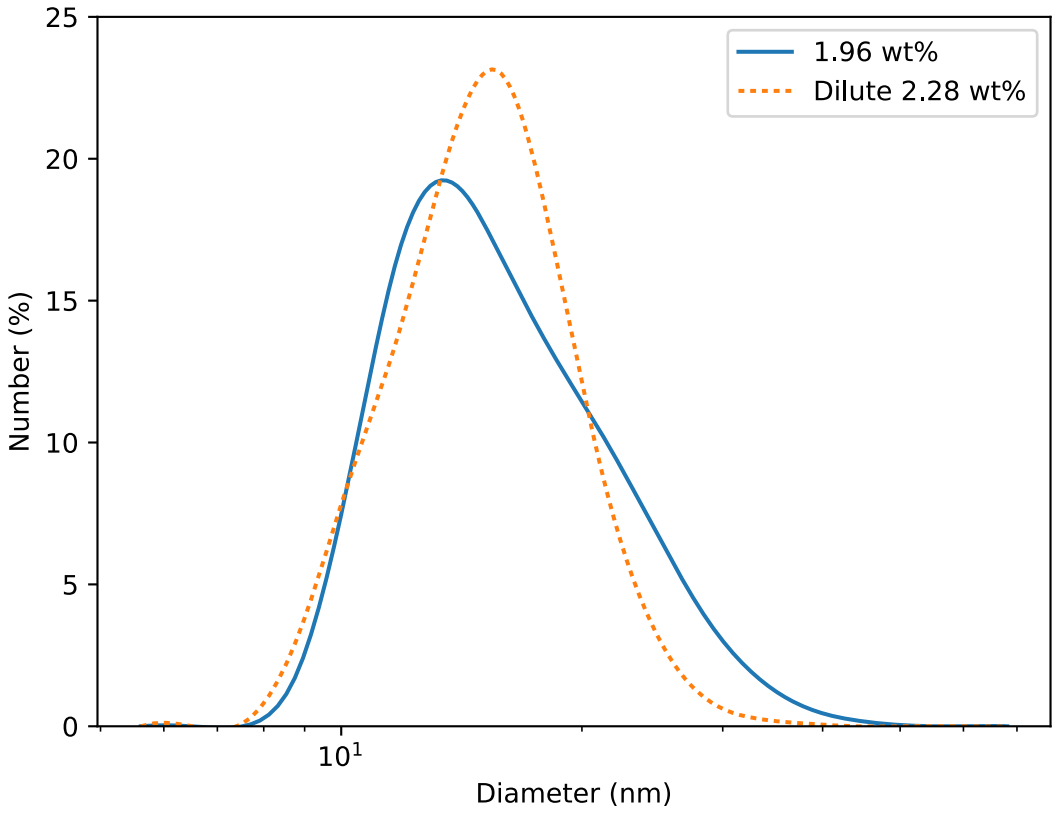

Figure 3-4 Size distribution of diluted 2.28 wt% starch nanoparticles dispersion and normal 1.96 wt% one.

3.2 Aging effect on starch nanoparticles dispersion

The production of starch nanoparticles dispersion need to be stored for future investigation, modification or application, thus the aging effect on the manipulated samples is required to be examined in order to make sure that the physical properties keep consistent in a reasonable shelf life.

Size distribution of diluted starch nanoparticles dispersion and viscosity of high concentration dispersion sample were chosen to test the aging effect on starch nanoparticles dispersion.

3.2.1 Aging effect on starch nanoparticles size

At low concentration, as above discussed, the starch nanoparticles dispersion is not aggregated, thus the size distribution is a normal distribution (like Figure 3-4) with only one peak. Based on these

observations, we can use the diameter of peak point to represent the size distribution, that is if the size of peak point changed significantly within time, there will be aging effect on starch nanoparticles size. On the contrary, we will get the conclusion that there is no aging effect on starch nanoparticles size if the diameter of peak point keep consistent in the examining period.

This study was based upon repeated measures designs. Three starch nanoparticles dispersion samples in different dilute concentration (1 wt%, 2 wt% and 3 wt%) were made and measured 6 times at every different date, and the results were shown in Table 3-2. Data are presented as quantile box plots (Figure 3-5, Figure 3-6 and Figure 3-7). The edges of the box represent the 25th and 75th percentiles, the median is a solid line through the box, outliers are represented as black diamond (♦), and the error bars represent the 95% confidence intervals.

Table 3-2 Diameter of the size distribution peak point data measured at different date.

Concentration	Diameter (nm)						
	15-Aug	16-Aug	17-Aug	18-Aug	25-Aug	26-Aug	13-Sep
1 wt%	9.28	20.13	20.23	12.40	19.29	17.63	17.10
	18.65	20.22	11.22	13.61	22.35	16.67	20.38
	13.58	19.23	13.29	19.84	20.80	10.78	18.99
	13.19	19.55	10.07	8.64	13.55	11.44	15.42
	8.51	13.20	15.25	17.32	20.33	12.04	10.84
	22.30	15.47	18.66	10.96	22.86	16.01	15.92
2 wt%	24.22	22.51	12.26	10.12	18.48	22.43	23.10
	10.68	15.93	14.00	24.00	22.09	23.04	12.81
	21.57	15.45	20.27	22.02	14.82	8.87	13.29
	19.86	18.92	16.41	11.63	18.09	11.15	10.85
	21.89	9.51	23.37	14.96	19.43	14.36	22.32
	17.92	17.47	20.74	12.90	11.93	18.33	7.99
3 wt%	10.47	4.69	13.02	8.59	15.73	14.99	9.82
	26.26	22.28	12.96	16.06	21.93	11.76	20.81
	19.64	20.94	17.34	14.08	13.72	13.85	15.45
	8.75	12.73	22.50	14.60	15.49	23.44	6.83
	15.12	18.51	14.09	16.35	13.40	10.75	12.93
	11.38	9.76	17.01	7.48	16.71	13.88	12.26

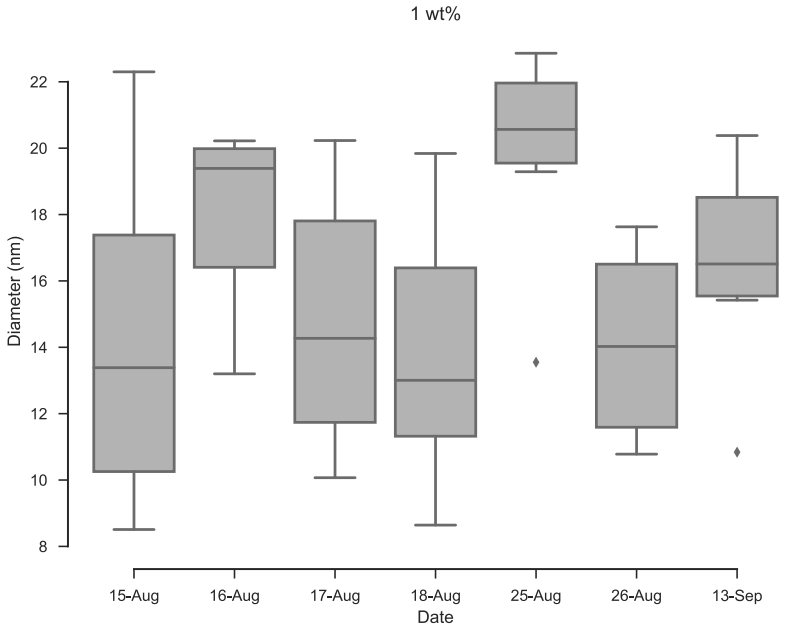

Figure 3-5 The peak diameter of 1 wt% starch nanoparticles dispersion were measured at different date.

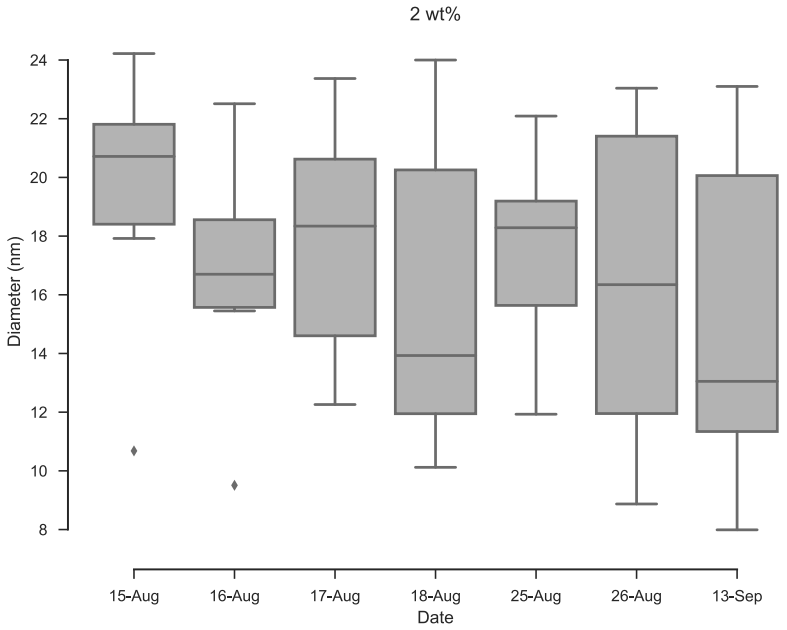

Figure 3-6 The peak diameter of 2 wt% starch nanoparticles dispersion were measured at different date.

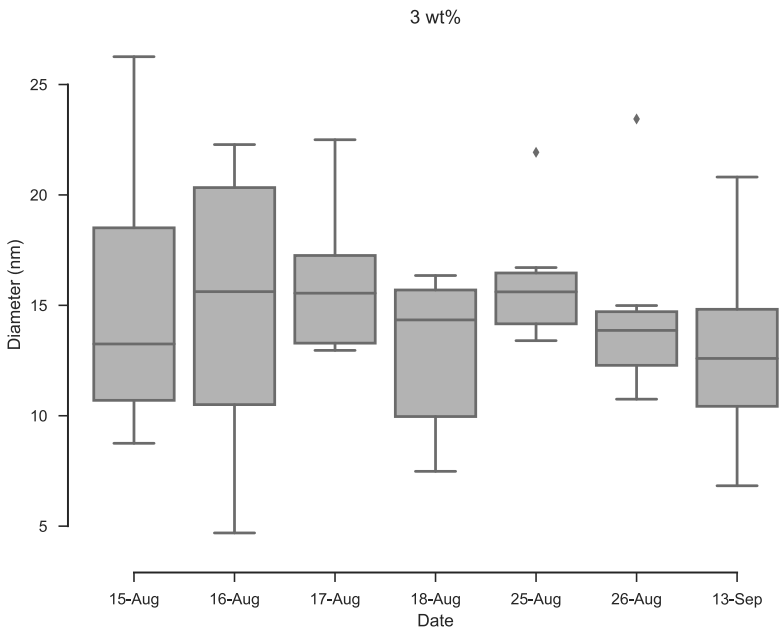

Figure 3-7 The peak diameter of 3 wt% starch nanoparticles dispersion were measured at different date.

As the results shown in these boxplots, it seems plausible that the measured diameters of peak keep were consistent around 10-20 nm from 15th Aug to 13th Sep, but it is hard to get the conclusion regarding the aging effect just by observation of raw eyes. In order to investigate this issue, analysis of variance (ANOVA), a sophisticated statistical analysis method, was applied. It mainly tested whether there were significant differences among diameters of peak point at each measuring date. In the meantime, we can also explore effect of dilute dispersion concentration on size distribution.

Table 3-3 ANOVA results for aging effect starch nanoparticles size.

Source value	Sum of squares	Degree of freedom	Mean square	F-value	P-value
Date	162.55	6	27.09	1.3016	0.2619
Concentration	104.42	2	52.21	2.5084	0.0858
Residual	2435.19	117	20.81		
Total	2702.16	125			

The ANOVA results for aging effect are given in Table 3-3. Since the two P-values were larger than 0.05, these factors had no statistically significant effect on the aging effect at the 95% confidence level that indicates a 5% risk of concluding that a difference exists when there is no actual difference. From the ANOVA tables given above, it is apparent that the F-values of factors date and concentration were less than $F_{0.05,6,117} = 2.1770$ and $F_{0.05,2,117} = 3.0738$ respectively.

To summarize, there was no peak shift after the dispersion produced, which denotes the nanoparticles size in dispersion is consistent over time and the size property of starch nanoparticles dispersion keeps stable for a reasonable period of time.

3.2.2 Aging effect on viscosity

Besides aging effect on dilute phase dispersion, we also want to understand the aging effect on the concentrated phase one. Because we cannot get the size distribution of concentrated starch nanoparticles dispersion based on the discussion of chapter 3.1, we will use viscosity as the probe to test the aging effect on high concentration dispersion.

The 30 wt% starch nanoparticles dispersion was prepared and stored in the lab that keeps 20 ^{o}C consistently, and the viscosity of same sample was measured at different date. As shown in the Figure 3-8, the data fluctuated within a certain reasonable range, from 600 to 1100 mPa·s, which indicates that the viscosity in dispersion is also consistent over time.

Apart from the aging effect, we can also find the viscosity remain constant no matter how fast the shear rate. In other word, viscosity is independent of the rate of shear. The relative topic will be discussed in detail in a subsequent section.

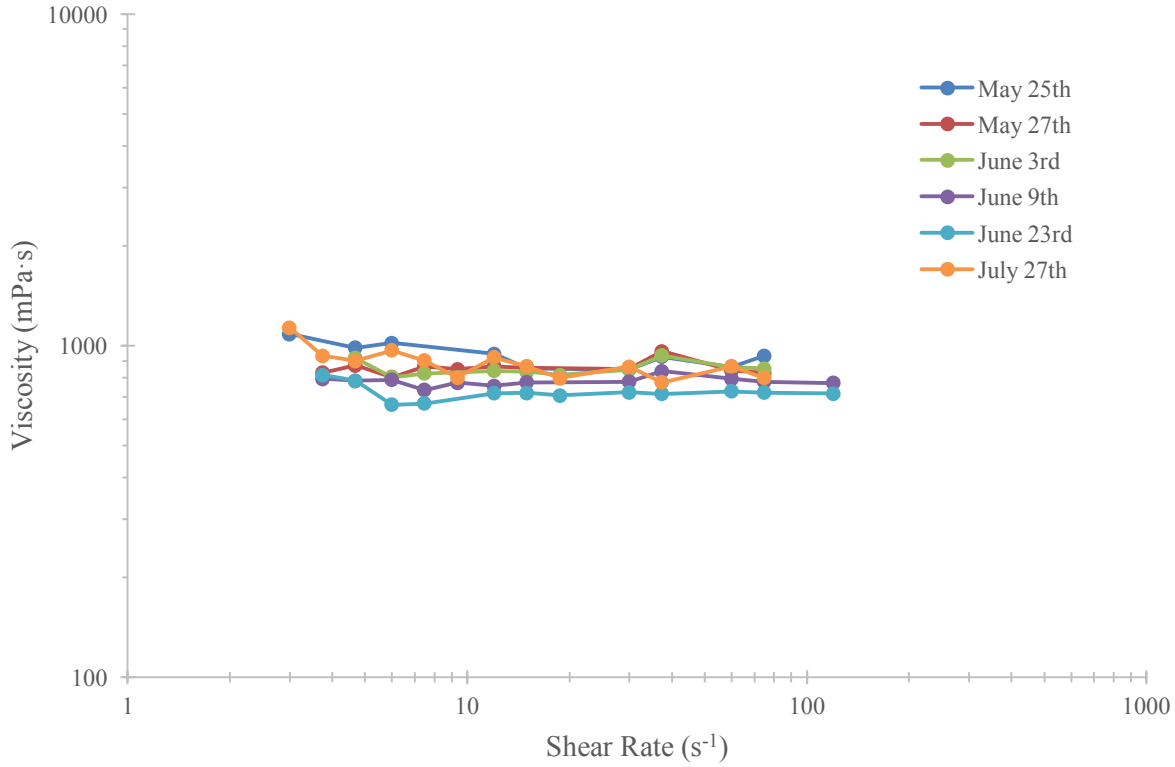

Figure 3-8 Aging effect on the viscosity of 30 wt% SNPs dispersion.

3.3 Swelling behavior of starch nanoparticle dispersion

The starch nanoparticle suspensions are prepared by dispersing the dry biopolymer nanoparticle agglomerates into water under agitation and shear mixing, in which the particles will absorb solution and form crosslinked water-swollen starch nanoparticles. Thus, it is important to examine the swelling behavior of the starch nanoparticles, which will provide more fundamental knowledge and details for future research and applications.

The relationship between volume fraction (volume occupied by particles per unit volume of dispersion) and relative viscosity plays an important role in understanding the swelling behavior of particles.

As we discussed in chapter 2.4, modified Einstein equation can be used to derive the swollenness of particles in the dilute phase.

For high concentration, there are several models try to describe the situation, Krieger & Dougherty equation is the most sophisticated model accepted by the relative researchers.

3.3.1 Swelling property on dilute phase

The relative viscosity ($\eta_r = \eta / \eta_o$) was measured by glass CANNON® Ubbelohde dilution viscometer (for the starch dispersion η and for its dispersion medium η_o that is water). And the volume fraction was derived from mass fraction. The detail calculation will be presented in the Appendix C.

The results are shown in Table 3-4 and plotted in Figure 3-9. Comparing with the B, Einstein coefficient, of rigid particles without swelling that is 2.5, the B came from the modified Einstein equation in the plot yields the swelling ratio:

$$swelling\ ratio = \frac{volume\ of\ swollen\ particles}{volume\ of\ dry\ particles} = \frac{38.69}{2.5} = 15.476$$

And the Ratio of swollen particle radius to dry particle radius is:

$$(\frac{38.69}{2.5})^{\frac{1}{3}} \approx 2.492$$

Table 3-4 Swelling property on dilute phase.

Volume Fraction	Relative Viscosity
0.0270	2.1250
0.0202	1.7500
0.0134	1.4500
0.0067	1.2000

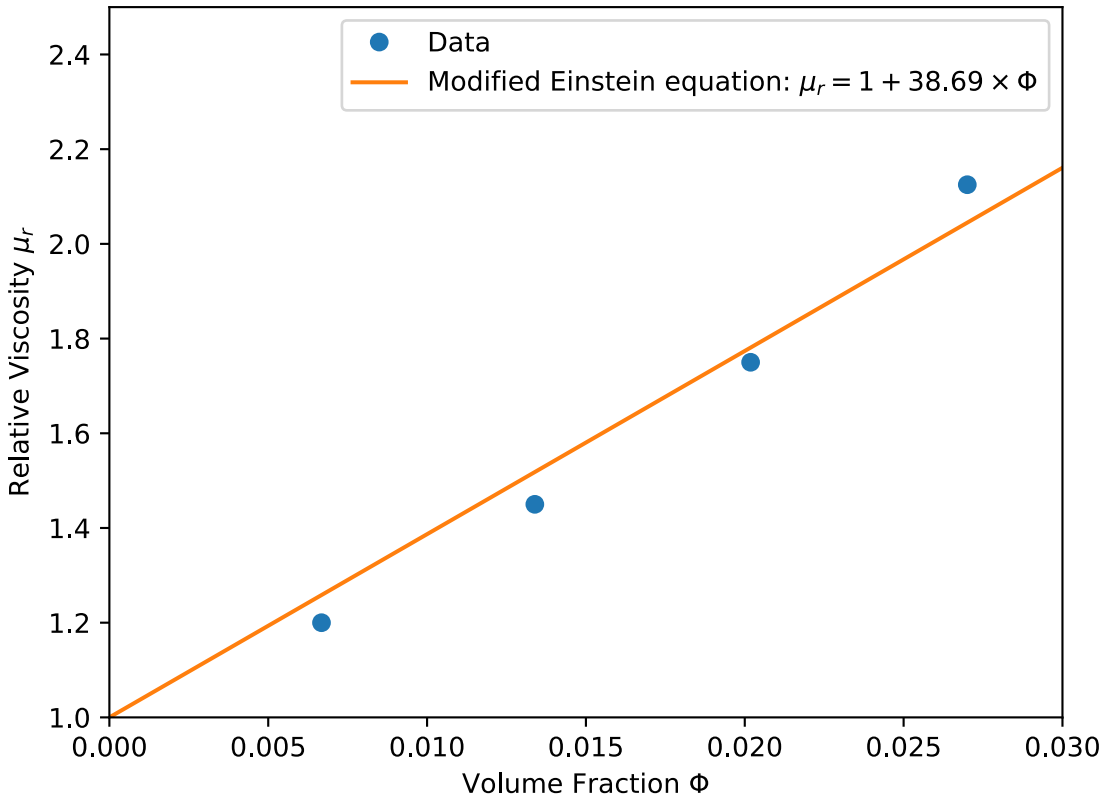

Figure 3-9 Swelling property on dilute phase.

3.3.2 Swelling property on concentrated phase

The data of swelling property on concentrated phase are shown in Table 3-5, which are plotted and regressed in Figure 3-10 based on the Krieger & Dougherty equation:

$$\eta_r = (1 - \frac{\emptyset}{\emptyset_m})^{-B\emptyset_m}$$

The B for concentrated phase is 21.49 from the Krieger & Dougherty equation in Figure 3-10, and similarly the welling ratio is:

$$swelling\ ratio = \frac{volume\ of\ swollen\ particles}{volume\ of\ dry\ particles} = \frac{21.49}{2.5} = 8.596$$

And the Ratio of swollen particle radius to dry particle radius is:

$$(\frac{38.69}{2.5})^{\frac{1}{3}} \approx 2.048$$

Table 3-5 Swelling property on concentrated phase.

Volume Fraction	Relative Viscosity
0.2677	1622.4522
0.2584	1226.6422
0.2414	929.8432
0.2333	684.1206
0.2242	642.9188
0.2138	310.5665
0.2026	264.0461
0.1832	223.7212
0.1731	142.5191
0.1632	97.1342
0.1436	67.3509
0.1244	37.0505
0.1055	23.8933
0.0870	15.6592
0.0688	9.7421
0.0581	7.0962
0.0548	5.1965
0.0478	4.1041
0.0408	3.3458
0.0339	2.7499
0.0270	2.1250
0.0202	1.7500
0.0134	1.4500
0.0067	1.2000

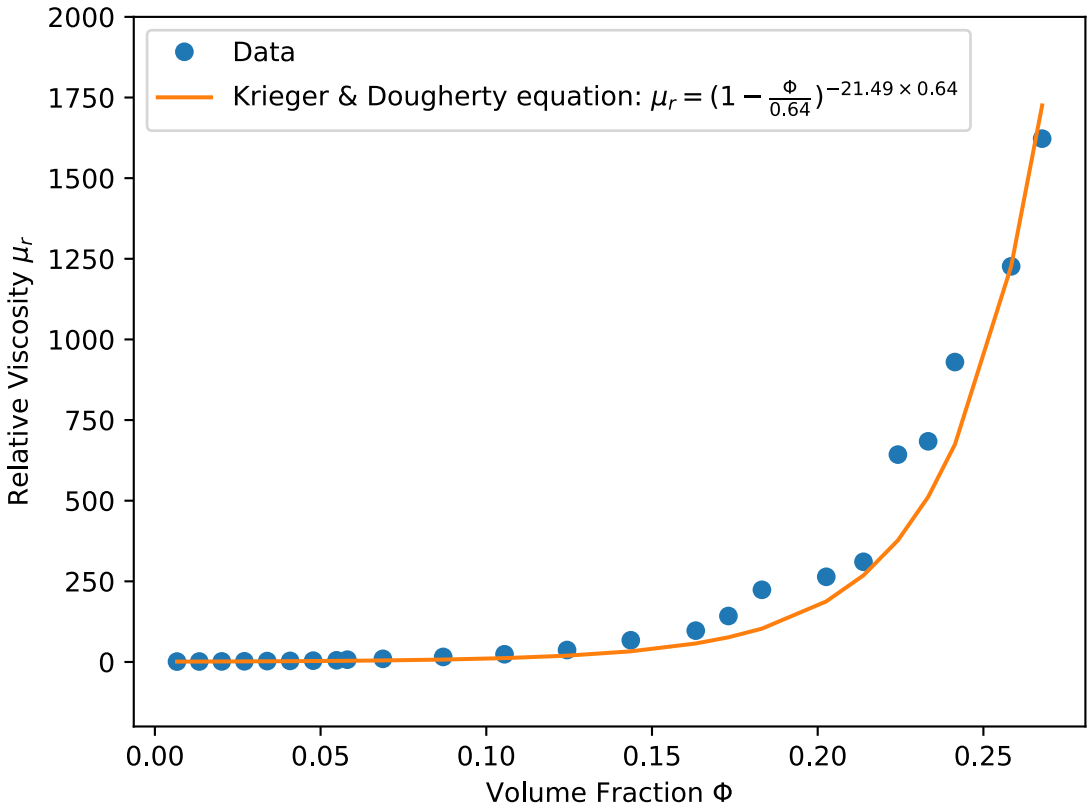

Figure 3-10 Swelling property on concentrated phase.

From the above results, we can find that the Einstein coefficient B varied at different concentration. Specifically, the B of dilute phase is larger than that of concentrated phase. In other word, the swelling behavior changed for different concentration starch nanoparticles dispersions. The swollen nanoparticles at dilute phase is larger than the swollen nanoparticles at concentrated phase.

The reason why this happen is shown in Figure 3-11. At low concentrations, the starch nanoparticles are completely swollen. Increasing the starch concentration eventually leads to a situation where the fully swollen granules just till up the available space. Finally, at high concentrations the amount of water becomes the limiting factor. Therefore, the starch nanoparticles cannot swell to their equilibrium volume.

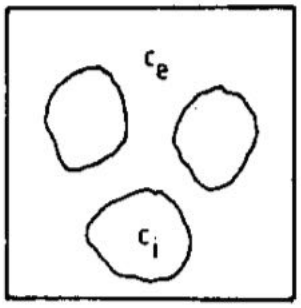

Dilute

Particles are swollen to equilibrium

$c_e = c_i$

$c_i = 1/q = c$

Volume fraction of particles = cq

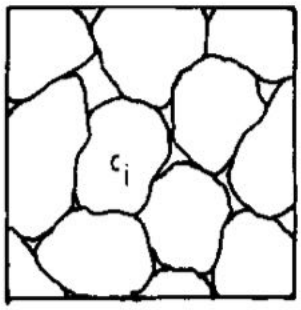

Transition region

Particles are swollen to equilibrium

$c_i = c = 1/q = c^*$

c^*= transition concentration

Volume fraction = cq = 1

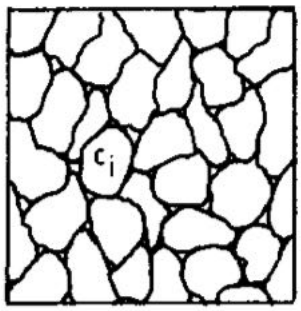

Concentrated

Particles swollen to less than equilibrium. System swells out at dilution

$c_i = c > c^*$

$cq > 1$

Figure 3-11 Concentration regimes in suspensions of gelatinised starch granules. C is the nominal starch concentration; C_e and C_i are concentration outside and inside swollen granules respectively; C^* is space-filling concentration; And q is equilibrium swelling volume.[49]

3.3.3 The effect of pH and concentration of salt on the swelling behavior of starch nanoparticle dispersion

It was observed that a high pH aqueous phase resulted in a faster dissolution rate of starch nanoparticles. In the meantime, salt was added into DI water, which makes pH adjustment more accurate. But there was no systemically examination of the effect of pH and salt on the swelling behavior of starch nanoparticles.

In order to investigate this question, factorial design was applied. This statistical tool has several important features in general. First, it is the most efficient way to study the effects of two or more factors. Second, it can examine all possible combinations of the levels of the factors. Finally, when factors are arranged in a factorial design, they are often said to be crossed.[50]

The 2^2 factorial design was used in this study, which is a factorial design with only two factors, say A and B, each run at two levels. The levels of the factors may be arbitrarily called "low" and "high." Table 3-6 gives the variable factors and their levels.

Table 3-6 Variables factorial design.

Factor	Factor levels	
	Low (-1)	High (+1)
pH	3	11
Salt concentration / mM	1	100

Using the following equation, the low and high level are coded by -1 and +1 respectively:

$$Coded\ Value = \frac{Uncoded\ Value - \frac{High + Low}{2}}{\frac{High - Low}{2}}$$

For instance, substituting pH = 3 into above equation yields:

$$Coded\ Value = \frac{3 - \frac{11 + 3}{2}}{\frac{11 - 3}{2}} = \frac{3 - 7}{4} = -1$$

Factor coding makes the two factors orthogonal. In other words, if factors are not coded, the cross-product terms in the regression model contain both interaction and main effects.

The results are shown in Table 3-7, from which we can find that there are four runs needed for the full factorial design (2^2). The starch nanoparticles dispersion was produced in the specific aqueous phase for each run, and the specific relative viscosity was measured by the method discussed in chapter 3.3.1, which yields the Einstein coefficient B by linear regression. The whole experiment was replicated three times.

Table 3-7 The results of Einstein coefficient B for the effect of pH and concentration of salt on the swelling behavior.

	Factor		B			
Run	Salt	pH	Replicate 1	Replicate 2	Replicate 3	Total
1	-1	-1	26.09	33.66	27.72	87.47
2	1	-1	24.59	31.16	27.28	83.02
3	-1	1	34.04	37.04	28.22	99.29
4	1	1	28.66	32.72	29.15	90.53

According to the experiments data, full factorial model is used to evaluate the effects of pH and salt concentration as follows:

	Main Effect		Interaction	
Run	Salt	pH	Salt & pH	Total
1	-1	-1	1	87.47
2	1	-1	-1	83.03
3	-1	1	-1	99.30
4	1	1	1	90.53

Based on these equations:

$$Contrast = \sum_{i=1}^{4} \lambda_i y_i$$

$$Effect = \frac{Contrast}{R2^{k-1}}$$

where i represents the number of run, λ is the coded value, y is the total of B, R is the time of replications and k is the number of factors, the effect estimate summary is calculated and shown in Table 3-8.

Table 3-8 Effect estimate summary.

Factor	Contrast	Effect
Salt	-13.21	-2.20
pH	19.33	3.22
Salt & pH	-4.32	-0.72

Using the calculated effects, the regression model is got as follow:

$$B = \frac{87.47 + 83.03 + 99.30 + 90.53}{4\times3} + \frac{-2.2}{2}\times Salt + \frac{3.22}{2}\times pH + \frac{-0.72}{2}\times(Salt \times pH)$$

Simplify the equation yields:

$$B = 30.03 - 1.1\times Salt + 1.61\times pH - 0.36\times(Salt \times pH)$$

The regression model is plotted in Figure 3-12, from which we can find that these two factors have very weak effect on the swelling behavior.

The ANOVA in Table 3-9 may be used to confirm the magnitude of these effects. We note from Table 3-9 that the main effects of pH and Salt are non-statistically significant (both P-values are larger than 0.05). The pH & Salt interaction is also non-statistically significant.

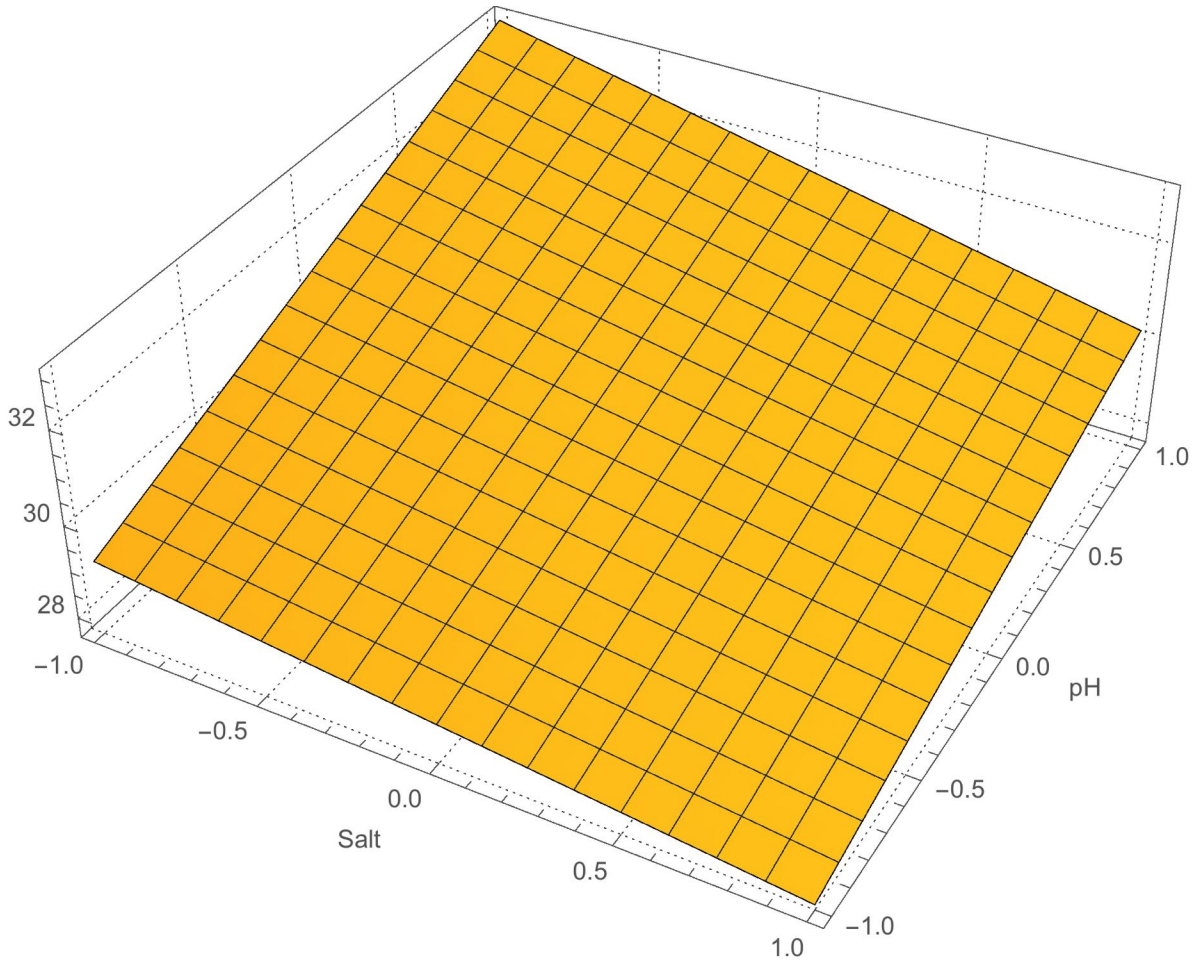

Figure 3-12 Response surface plot.

Table 3-9 Analysis of variance for the Einstein coefficient on swelling behavior.

Source value	Sum of squares	Degree of freedom	Mean square	F-value	P-value
Salt	14.53	1	14.53	1.12	0.32
pH	31.14	1	31.14	2.40	0.16
Salt x pH	1.55	1	1.55	0.12	0.74
Residual	103.65	8	12.96		
Total	150.88	11	13.72		

3.4 Rheology of starch nanoparticle dispersion

In chapter 3.2.2, we discussed the aging effect on high concentrated dispersion by shear viscosity. The rheology of starch nanoparticles dispersion will be systematically examined in this chapter, specifically, we explored the effect of temperature and concentration on the rheology.

Shear viscosity was mainly measured by using a stress control type rheometer, i.e. Rotovisco® RV 12 from HAAKE with rotor-bob geometry system MV I (shear rate up to 1198 s-1). The temperature was kept at room temperature 21 ℃ except when examining the temperature effect.

3.4.1 Effect of temperature

Shear viscosity of 30 wt% starch nanoparticles dispersion as a function of shear rate and temperatures is plotted in Figure 3-13.

It can be seen in Figure 3-13 that the viscosity is uncorrelated with shear rate, which implies the starch nanoparticles dispersion is Newtonian fluid at the examined shear rate range. The reason why the shear rate range is not same at different temperature is that the viscosity is indirectly measured by torque which has 0-100 measure range and calculated by relative transforming equations, and more details are presented in the appendix part.

Based on the experiment data, the average shear viscosity was calculated in Table 3-10 and plotted in Figure 3-14, in which it can be observed that there is a certain non-linear negative relationship between shear viscosity and temperature in starch nanoparticles dispersion: the viscosity for starch nanoparticles dispersion is decreased by temperature.

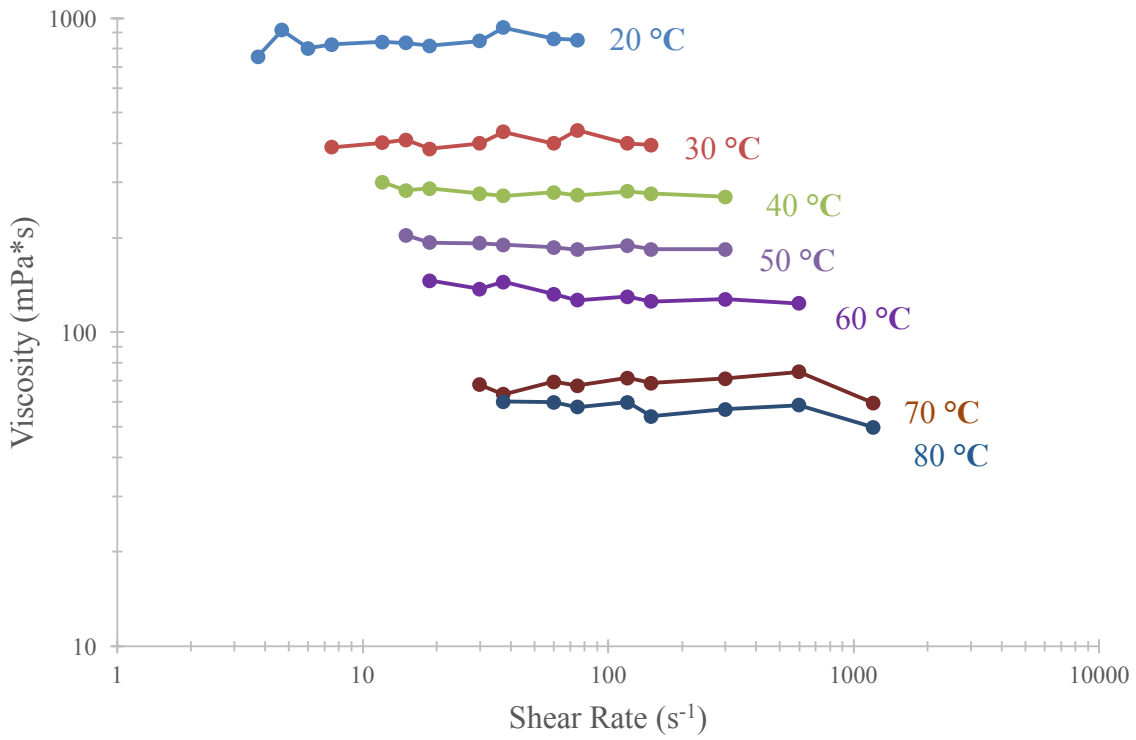

Figure 3-13 Relationship between shear viscosity and shear rate of 30 wt% starch nanoparticles dispersion at various temperature.

Table 3-10 Shear viscosity of 30 wt% starch nanoparticles dispersion at various temperature.

Temperature (°C)	Viscosity (mPa·s)	Standard deviation
20	843.72	49.58
30	405.15	18.63
40	279.85	8.89
50	189.45	6.49
60	132.54	8.28
70	68.28	4.49
80	57.09	3.56

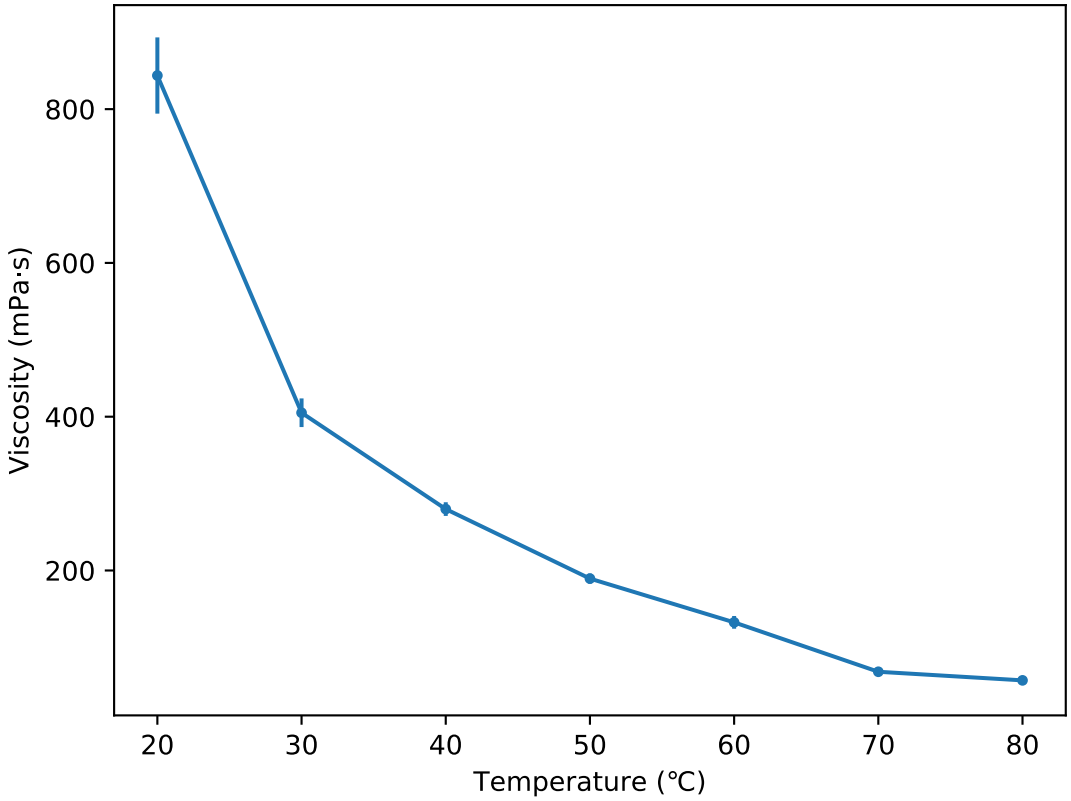

Figure 3-14 Relationship between shear viscosity and temperature of 30 wt% starch nanoparticles dispersions.

3.4.2 Effect of concentration

Figure 3-15 shows the results for the starch nanoparticles dispersion where the viscosity in mPa·s determined at 21 °C is plotted against shear rate for each of the different concentration. Similarly, the average shear viscosity was calculated in Table 3-11 based on these data and typical viscosity-concentration results for starch nanoparticles dispersions are shown in Figure 3-16.

It can be observed that there is a certain non-linear positive relationship between shear viscosity and concentration in starch nanoparticles dispersion: the viscosity for starch nanoparticles dispersion is increased by concentration.

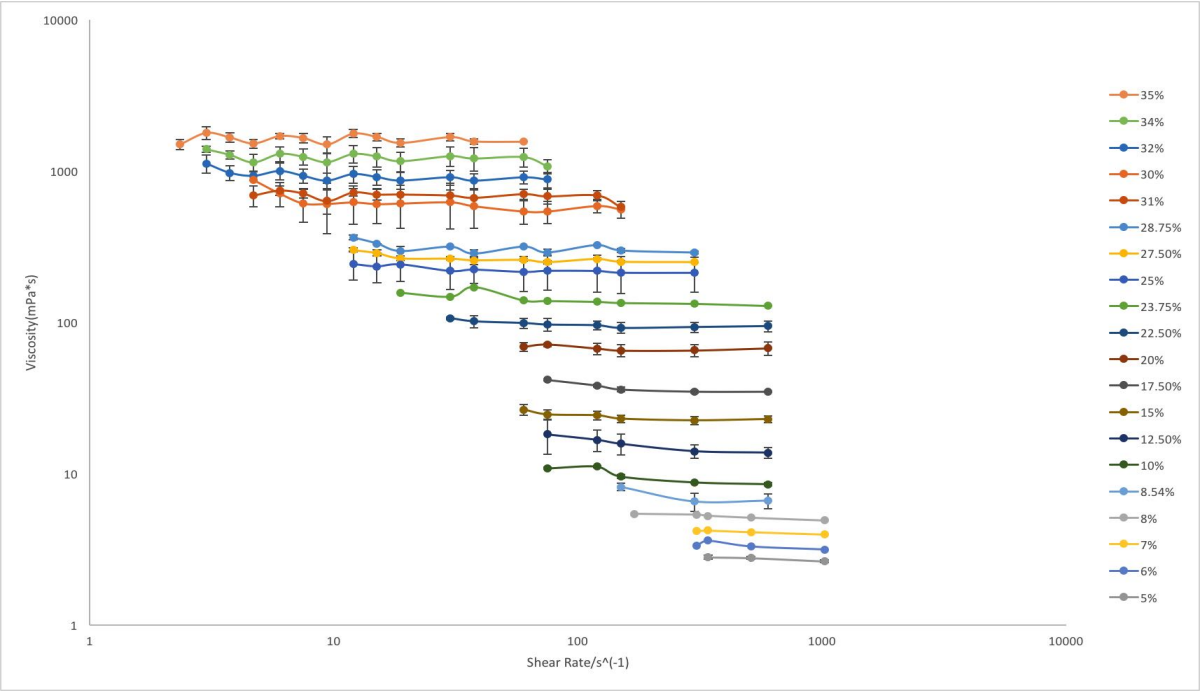

Figure 3-15 Relationship between shear viscosity and shear rate of starch nanoparticles dispersion at various concentration.

Table 3-11 Shear viscosity of starch nanoparticles dispersion at various concentration.

Concentration (wt%)	Viscosity (mPa·s)	Standard deviation
35.00%	1622.45	100.97
34.00%	1226.64	84.87
32.00%	929.84	70.26
31.00%	684.12	41.32
30.00%	620.39	87.12
28.75%	310.57	24.33
27.50%	264.05	16.87
25.00%	223.72	11.33
23.75%	142.52	13.22
22.50%	97.13	4.79
20.00%	67.35	2.24
17.50%	37.05	2.91
15.00%	23.89	1.46
12.50%	15.66	1.85

10.00%	9.74	1.21
8.54%	7.10	0.92
8.00%	5.20	0.20
7.00%	4.10	0.11
6.00%	3.35	0.19
5.00%	2.73	0.09

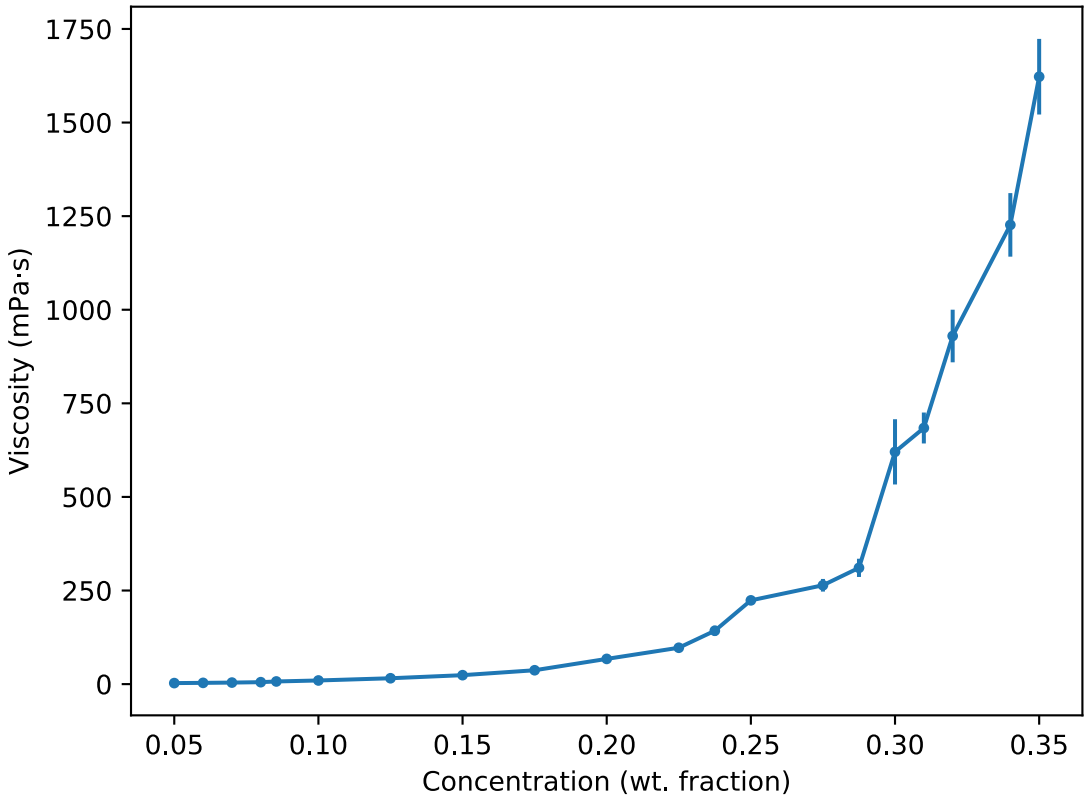

Figure 3-16 Relationship between shear viscosity and concentration of starch nanoparticles dispersions at 21 °C.

3.5 Flow behavior of starch nanoparticle dispersion in pipelines

All fluid flow is classified into one of two broad categories or regimes: laminar flow or turbulent flow. When the fluid particles flow without intersecting the paths of each other and the velocity of the particle is always tangential to the path of the particle, the flow is said to be a laminar flow. In other word, laminar flow occurs at low velocities and low Reynolds number, and the path of the fluid lines is regular and streamline where there is no lateral disturbance of the fluid paths and the fluid flows in layers.

On the contrary, when the fluid properties, pressure and flow velocity, in a flow vary rapidly with time, the flow is known as a turbulent flow. That is turbulence flow occurs at high velocities and high Reynolds number, and the flow pattern is irregular and chaotic, where vortices, eddies, and cross currents occur.

Figure 3-17 shows the different structure of laminar flow and turbulent flow in pipelines. Both laminar flow and turbulent flow the shear stress can be described by the applied shearing force over the surface area to which the force is applied.

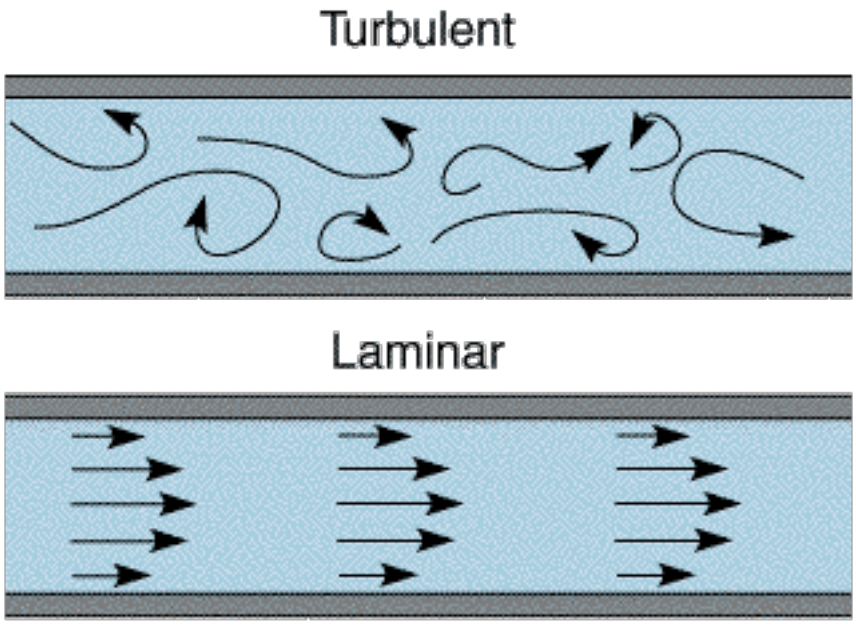

Figure 3-17 Different structures between laminar flow and turbulent flow.[51]

Because a certain amount of energy is consumed to overcome the wall friction when fluid flows through pipelines, the formula to calculate the wall shear stress (τ_w) in fully developed pipe flow is:

$$\tau_w = \frac{\Delta P * D}{4L} \tag{3.1}$$

where ΔP is pressure drop, L is the test section length and D is the diameter of the pipeline.

The Fanning friction factor is defined as:

$$f = \frac{\tau_w}{\frac{1}{2}\rho V^2} \tag{3.2}$$

where ρ is the density of fluid and V is the mean flow velocity.

Substituting equation (3.1) into above equation yields:

$$f = \frac{\Delta \mathrm{P} * \mathrm{D}}{2\rho V^2 L} \tag{3.3}$$

V cannot be directly measured in our experiment, so we use volumetric flow rate (Q) to represent V based on the following equations:

$$V = \frac{Q}{A} \tag{3.4}$$

$$A = \frac{1}{4}\pi D^2 \tag{3.5}$$

Substituting equation (3.4) and (3.5) into equation (3.3) yields:

$$f = \frac{\pi^2 D^5 \Delta P}{32\rho L Q^2} \tag{3.6}$$

For flow in a pipe or tube, the Reynolds number is generally defined as:

$$\mathrm{Re} = \frac{QD}{\nu A} \tag{3.7}$$

where ν is the kinematic viscosity and defined as:

$$\nu = \frac{\mu}{\rho} \tag{3.8}$$

where μ is the dynamic viscosity of the fluid.

Substituting equation (3.4) and (3.8) into equation (3.7) yields:

$$\mathrm{Re} = \frac{4Q\rho}{\pi\mu D} \tag{3.9}$$

In summary, f and Re in our experiment were calculated by equation (3.6) and equation (3.9) respectively, and the calculation detail will be presented in the Appendix C.

Figure 3-18 shows a schematic friction factor behaviour in which the friction factor is plotted versus the Reynolds number of a pipe flow. The skeleton of such diagrams are the curves for a Newtonian fluid in a pipe with smooth walls.

The friction factor for laminar flow of Newtonian fluids in round tubes is often taken to be:[52]

$$f = \frac{16}{Re} \tag{3.10}$$

Prandtl-von Kannan law[53] is the most common representation of turbulent flow of Newtonian fluids and is given by:

$$f^{-0.5} = 4\, log_{10}(Re * f^{0.5}) - 0.4 \tag{3.11}$$

which works over a large range of Reynolds numbers: roughly from 2.1×10^3 to 5×10^6.

Alternatively, the friction factor for turbulent flow of Newtonian fluid in smooth pipes can be estimated by some simple empirical equations. Three different equations have been experimentally developed and all of them can be shown in the same form:

$$f = a + \frac{b}{Re^n} \tag{3.12}$$

Table 3-12 shows the equation names and relative parameter values.

Table 3-12 Empirical equation coefficients for turbulent flow with Re.[47]

Equation name	a	b	n	Re range	
Blasius	0	0.079	0.25	4×10^3	1×10^5
Colburn	0	0.046	0.2	1×10^5	1×10^6
Koo	0.0014	0.125	0.32	4×10^3	3×10^6

The Blasius equation is the most popular one to represent turbulent flow behavior as plotted in the Figure 3-18, and Koo equation is more accurate at larger Re range.

Drag reduction was discovered as a reduction in the pressure drop of the flow of a turbulent pipe flow at the same flow rate due to additives, for instance flexible polymer, surfactant and fibre solutions. A definition of drag reduction is "drag reduction is the reduction of skin friction in turbulent flow below that of the solvent", which was proposed by Lumley at 1969.[53]

The drag reduction can be examined by comparing the gap between experiment data and Blasius equation when analyzing and plotting the raw data into Figure 3-18.

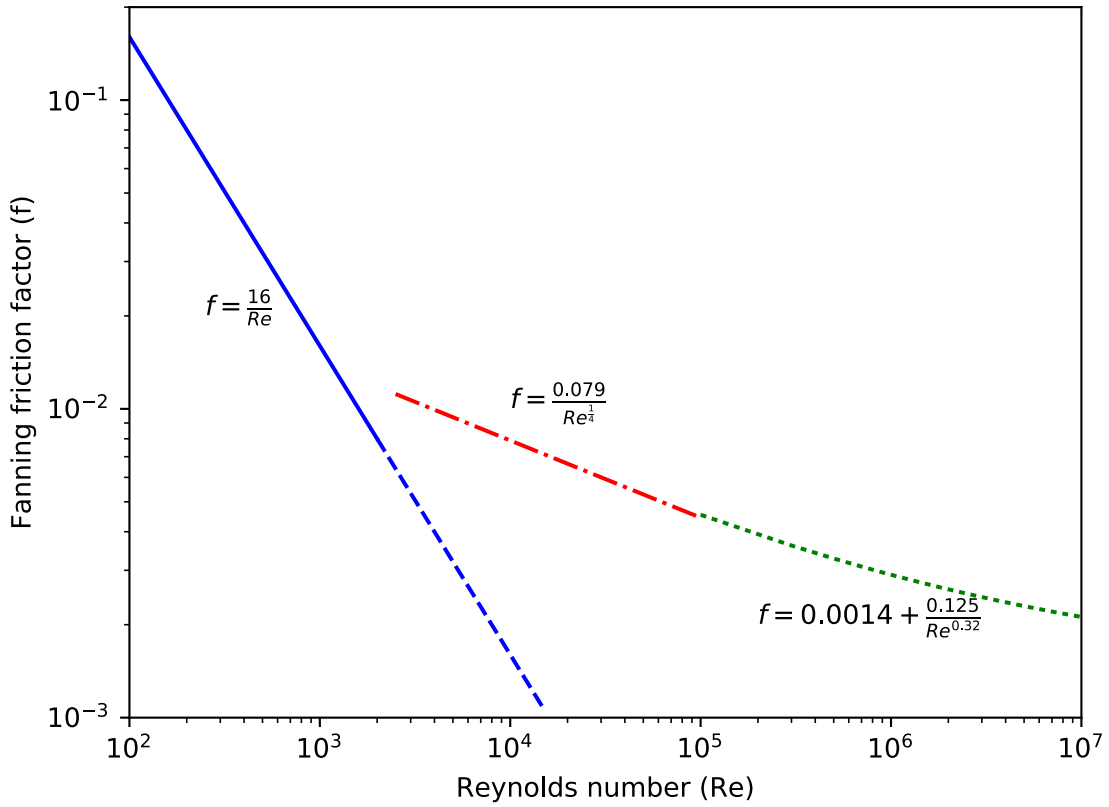

Figure 3-18 Fanning friction factor for tube flow: blue solid line represents laminar pipe flow; red dash-dotted line represents turbulent pipe flow.

Figure 3-19 and Figure 3-20 present the pipeline behavior of starch nanoparticles dispersion with respect to Reynolds number in the 1-inch pipe. Different concentration starch nanoparticles dispersion flow data are separately shown on the Figure 3-19, and compared on the Figure 3-20. It is obvious that whatever the concentration of starch nanoparticles dispersion, the flow data followed the Blasius equation, which means no drag reduction was observed for starch nanoparticles dispersion at these concentration levels.

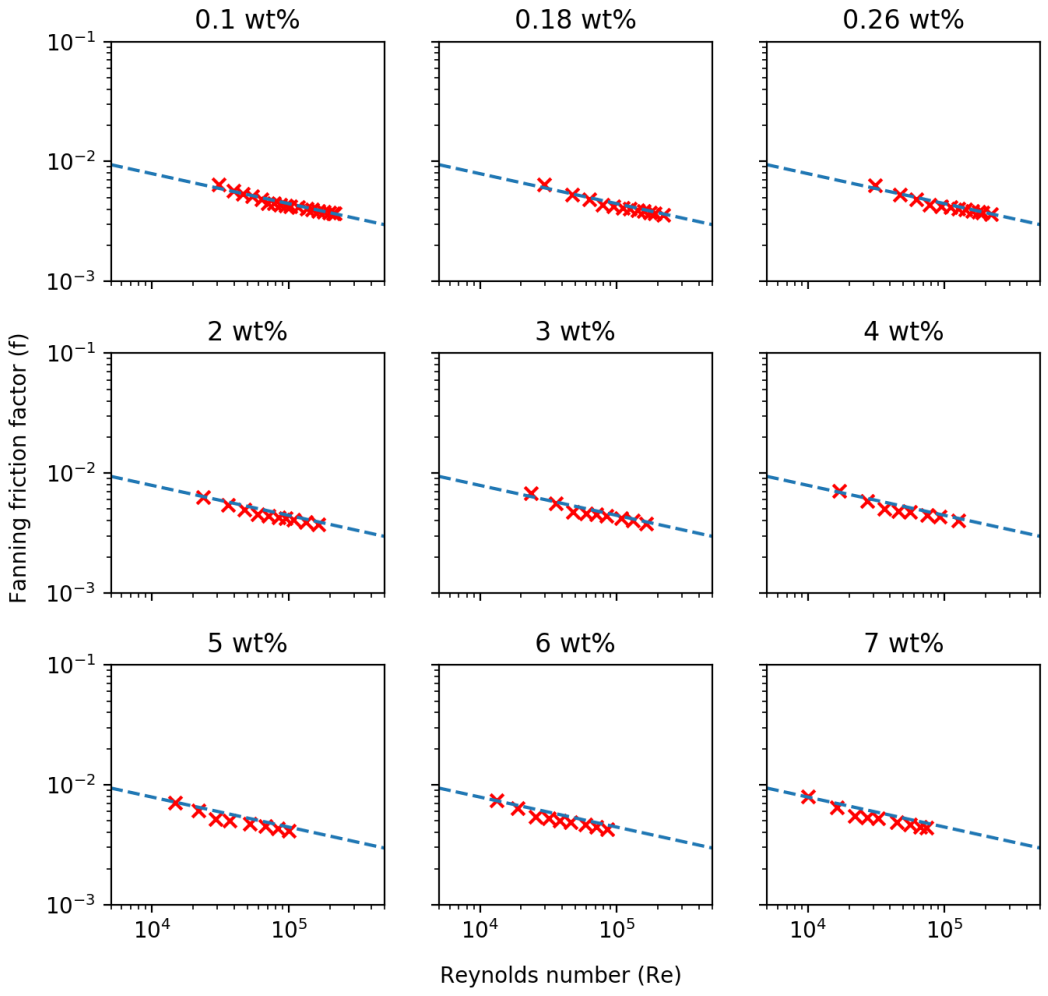

Figure 3-19 Friction factor vs. Reynolds number plot for starch nanoparticles dispersion at different concentration in 1 inch pipe, where marker 'x' represents the experiment data and dashed line is the Blasius equation.

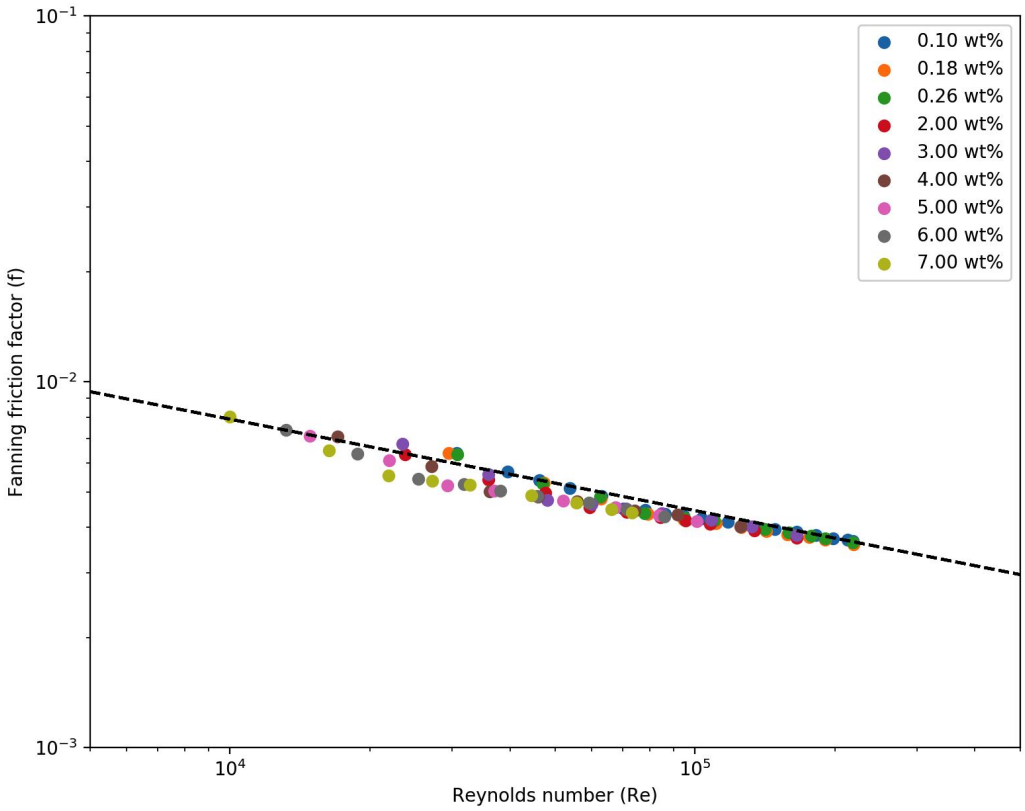

Figure 3-20 Friction factor vs. Reynolds number plot for starch nanoparticles dispersion at different concentration in 1 inch pipe, where dashed line represents the Blasius equation.

3.6 Surface tension of starch nanoparticle dispersion

Surface tensions were measured for the starch nanoparticles dispersion using CSC precision and interfacial DuNouy tensiometers at room temperature (21 ^{o}C). As shown in Figure 3-21, water has a much higher surface tension (71 dyne/cm) compared to starch nanoparticles dispersion, which implies that the starch nanoparticles can decrease the surface tension of water-air system. And our measurements indicate that in starch nanoparticles dispersion the surface tension keep consistent within dilute and medium concentration.

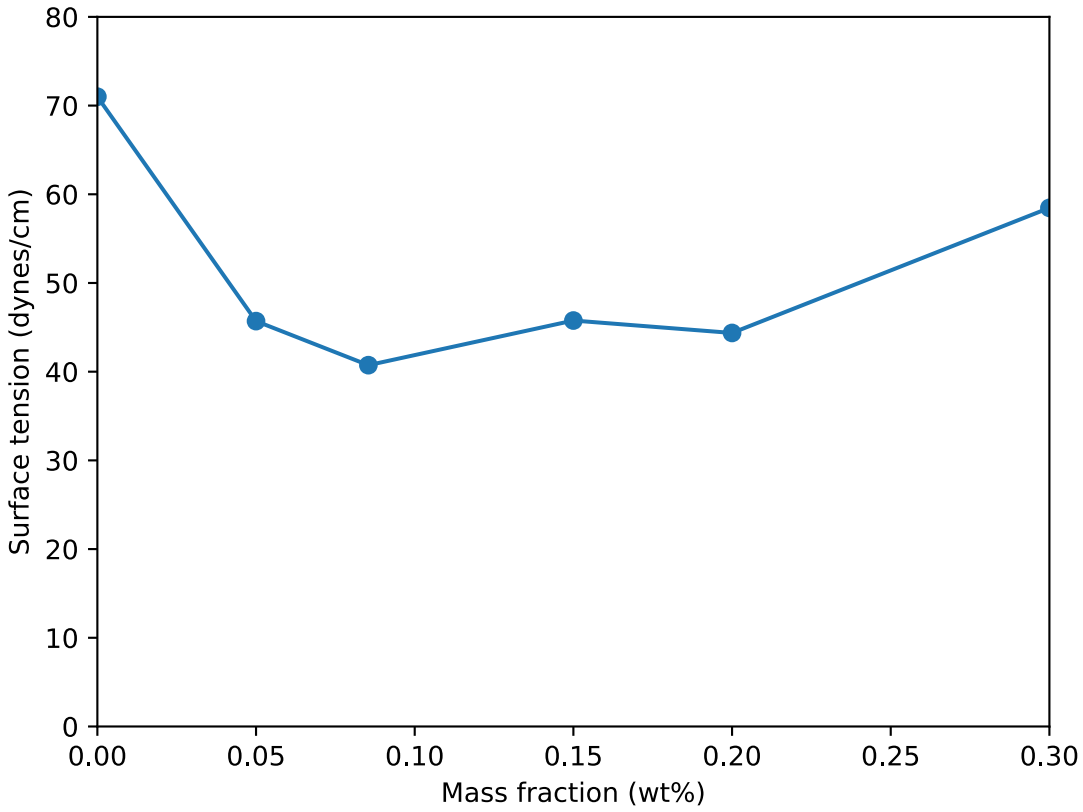

Figure 3-21 Variation in the surface tension of starch nanoparticles dispersion with increasing mass fraction.

3.7 Conductivity of starch nanoparticle dispersion

Figure 3-22 describes the relationship between conductivity and mass friction in starch nanoparticles dispersion. Although there was an upside-down U-shape trend, the conductivity remained very low. As compare, the conductivity of 0.01M NaCl was 1121 μS/cm, but the maximum conductivity of starch nanoparticles dispersion was only less than 400 μS/cm.

Based on the above result, we can conclude that starch nanoparticles have a very weak effect on the conductivity of starch nanoparticle dispersion.

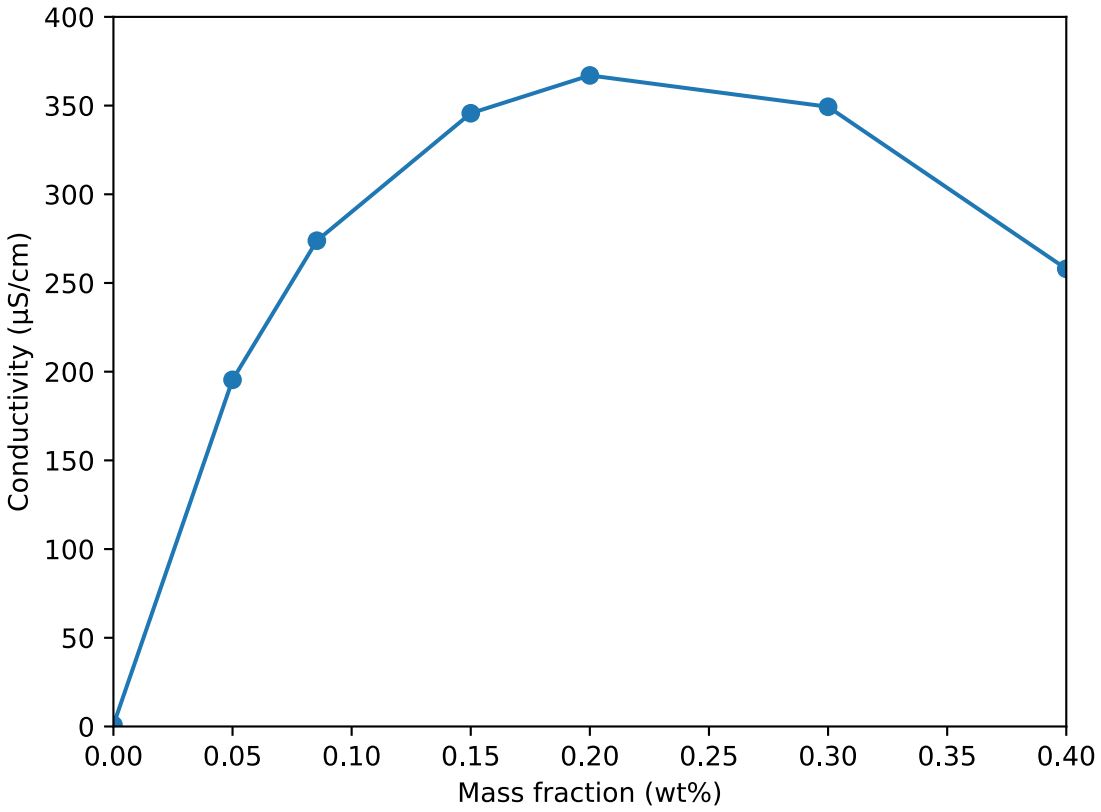

Figure 3-22 Variation in the conductivity of starch nanoparticles dispersion with increasing mass fraction.

3.8 Zeta potential of starch nanoparticles dispersion

The zeta potential value of 1 wt% starch nanoparticles dispersion was 3.96 mV and the zeta potential distribution was plotted in Figure 3-23. Normally the values of zeta potential more positive than 30 mV or more negative than 30 mV are electrochemically stable, but the starch nanoparticles dispersion in our research is sort of stable when the zeta potential value is only 3.96 mV. This is a very interesting phenomena and maybe further investigations can be done in this area.

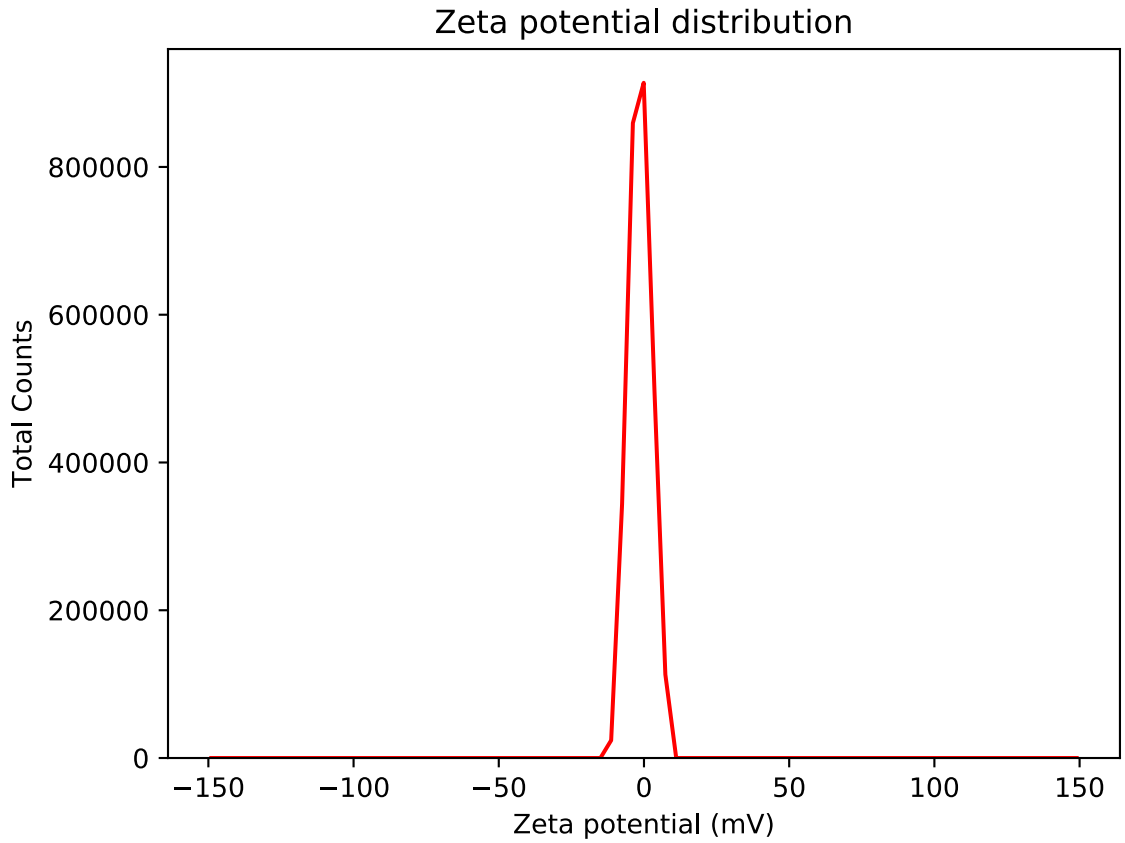

Figure 3-23 Zeta potential distribution of 1 wt% starch nanoparticles dispersion.

Chapter 4
Conclusions and Recommendations

4.1 Conclusions

Starch nanoparticles are promising material and have potential applications in various regions including agriculture, pharmaceutical industry and oil extraction. The fundamental physical properties of starch nanoparticles were systematically examined in our research.

First of all, size distribution of starch nanoparticles dispersion was investigated, by which we found that the peaks of particle size distribution shifted towards a larger number with increasing the mass fraction of starch particles, because of aggregation of starch nanoparticles. Although the nanoparticles will automatically aggregate into larger particles at medium and high concentration, there was no permanent aggregation in the starch nanoparticle dispersion system.

Secondly, aging effect of starch nanoparticle dispersion was thoroughly explored during this project. There is no aging effect on particle size, which means the size of starch nanoparticles in the dilute dispersion kept consistent after producing. In the meantime, there is no aging effect on viscosity either, in other word, the viscosity of starch nanoparticles dispersion at high concentration kept consistent after producing. Based on these experiments results, it was concluded that the starch nanoparticles dispersion is stable in a reasonable time period.

Moreover, swelling property of starch nanoparticle suspension was evaluated at different concentration and various preparation conditions. Above all, salt concentration and pH have no statistically significant effect on the swelling property of starch nanoparticles dispersion. And swelling property of starch nanoparticle dispersion at dilute phase and concentrated phase are different. Specifically, starch nanoparticles are swollen to equilibrium at dilute phase but to less than equilibrium at concentrated phase.

In addition, the rheology of starch nanoparticles dispersion was analyzed at different temperature and various concentration. The viscosity of starch suspension decreases with increasing the temperature and increases with increasing the concentration.

Pipe behavior was studied by pumping the starch nanoparticles dispersion in the flow loop. The pumping behavior of starch nanoparticles dispersion is not significantly different from water via

comparing the experiment data with Blasius equation, which represents that there is no drag reduction effect of starch nanoparticles.

Finally, the surface tension and conductivity of starch nanoparticles dispersion were measured at different concentration. Based on the results, it is found that the starch nanoparticles can lower the surface tension between water and gas and have a very weak effect on the conductivity.

4.2 Recommendations

The results discussed above are all based on one fundamental assumption that the shape of starch nanoparticles is a ball. If we can directly observe the sample's shape and surface topography by the advanced microscope technology, for instance scanning electron microscope (SEM), then we will have more knowledge and insights to analyze and examine the property of the starch nanoparticles.

Given the basic property examination of starch nanoparticles, developing the applications of this kind of starch nanoparticle, for example oil extraction, will be feasible in the future.

The modification of starch nanoparticles will provide some specific properties at different application area. We can use the knowledge we already got to lead our modification and extend our research into the modified starch nanoparticles.

Bibliography

1. Le Corre D, Bras J, Dufresne A. Starch Nanoparticles: A Review. *Biomacromolecules*. 2010;11(5):1139-1153. doi:10.1021/bm901428y.

2. Sajilata M g., Singhal RS, Kulkarni PR. Resistant Starch–A Review. *Compr Rev Food Sci Food Saf*. 2006;5(1):1-17. doi:10.1111/j.1541-4337.2006.tb00076.x.

3. Angellier H, Choisnard L, Molina-Boisseau S, Ozil P, Dufresne A. Optimization of the Preparation of Aqueous Suspensions of Waxy Maize Starch Nanocrystals Using a Response Surface Methodology. *Biomacromolecules*. 2004;5(4):1545-1551. doi:10.1021/bm049914u.

4. Vaclavik V, Christian EW. *Essentials of Food Science*. Springer Science & Business Media; 2007.

5. Global Starch And Derivatives Market To Grow To $77.4 Billion By 2018: BCC Research. http://www.bccresearch.com/pressroom/fod/global-starch-derivatives-market-grow-$77.4-billion-2018. Accessed December 16, 2016.

6. Buléon A, Colonna P, Planchot V, Ball S. Starch granules: structure and biosynthesis. *Int J Biol Macromol*. 1998;23(2):85-112. doi:10.1016/S0141-8130(98)00040-3.

7. French D. Organization of starch granules. *Starch Chem Technol*. 1984;2:183–247.

8. Gallant DJ, Bouchet B, Baldwin PM. Microscopy of starch: evidence of a new level of granule organization. *Carbohydr Polym*. 1997;32(3):177–191.

9. BeMiller JN, Whistler RL. *Starch: Chemistry and Technology*. Academic Press; 2009.

10. Vandeputte GE, Delcour JA. From sucrose to starch granule to starch physical behaviour: a focus on rice starch. *Carbohydr Polym*. 2004;58(3):245-266. doi:10.1016/j.carbpol.2004.06.003.

11. Oates CG. Towards an understanding of starch granule structure and hydrolysis. *Trends Food Sci Technol*. 1997;8(11):375-382. doi:10.1016/S0924-2244(97)01090-X.

12. Imberty A, Perez S. A revisit to the three-dimensional structure of B-type starch. *Biopolymers*. 1988;27(8):1205-1221. doi:10.1002/bip.360270803.

13. Imberty A, Chanzy H, Perez S, Buleon A, Tran V. New three-dimensional structure for A-type starch. *Macromolecules*. 1987;20(10):2634-2636. doi:10.1021/ma00176a054.

14. Cornuéjols D. The levels of starch organisation. http://www.scienceinschool.org/2010/issue14/starch. Accessed January 16, 2017.

15. Lamanna M, Morales NJ, García NL, Goyanes S. Development and characterization of starch nanoparticles by gamma radiation: Potential application as starch matrix filler. *Carbohydr Polym*. 2013;97(1):90-97. doi:10.1016/j.carbpol.2013.04.081.

16. Kim J-Y, Lim S-T. Preparation of nano-sized starch particles by complex formation with n-butanol. *Carbohydr Polym*. 2009;76(1):110-116. doi:10.1016/j.carbpol.2008.09.030.

17. Tan Y, Xu K, Li L, Liu C, Song C, Wang P. Fabrication of Size-Controlled Starch-Based Nanospheres by Nanoprecipitation. *ACS Appl Mater Interfaces*. 2009;1(4):956-959. doi:10.1021/am900054f.

18. Ma X, Jian R, Chang PR, Yu J. Fabrication and Characterization of Citric Acid-Modified Starch Nanoparticles/Plasticized-Starch Composites. *Biomacromolecules*. 2008;9(11):3314-3320. doi:10.1021/bm800987c.

19. Bloembergen S, Lee D. In: Atlanta: TAPPI PaperCon; 2010:18.

20. Song D, Thio YS, Deng Y. Starch nanoparticle formation via reactive extrusion and related mechanism study. *Carbohydr Polym*. 2011;85(1):208-214. doi:10.1016/j.carbpol.2011.02.016.

21. Liu D, Wu Q, Chen H, Chang PR. Transitional properties of starch colloid with particle size reduction from micro- to nanometer. *J Colloid Interface Sci*. 2009;339(1):117-124. doi:10.1016/j.jcis.2009.07.035.

22. Dufresne A, Thomas S, Pothan LA. *Biopolymer Nanocomposites: Processing, Properties, and Applications*. John Wiley & Sons; 2013.

23. Biliaderis CG, Grant DR, Vose JR. Structural characterization of legume starches. I. Studies on amylose, amylopectin, and beta-limit dextrins. *Cereal Chem USA*. 1981. http://agris.fao.org/agris-search/search.do?recordID=US8129489. Accessed January 24, 2017.

24. Jayakody L, Hoover R. The effect of lintnerization on cereal starch granules. *Food Res Int*. 2002;35(7):665-680. doi:10.1016/S0963-9969(01)00204-6.

25. Angellier H. Material Sciences. *Univ Joseph Fourier Grenoble Fr*. 2005:285.

26. Singh V, Ali SZ. Acid degradation of starch. The effect of acid and starch type. *Carbohydr Polym*. 2000;41(2):191-195. doi:10.1016/S0144-8617(99)00086-7.

27. Kim J-Y, Park D-J, Lim S-T. Fragmentation of waxy rice starch granules by enzymatic hydrolysis. *Cereal Chem*. 2008;85(2):182–187.

28. Gallant D. Contribution à l'étude de la structure et de l'ultrastructure du grain d'amidon. 1974. http://kbd.kew.org/kbd/detailedresult.do?id=39551. Accessed January 24, 2017.

29. Chin SF, Pang SC, Tay SH. Size controlled synthesis of starch nanoparticles by a simple nanoprecipitation method. *Carbohydr Polym*. 2011;86(4):1817-1819. doi:10.1016/j.carbpol.2011.07.012.

30. Shi A, Li D, Wang L, Li B, Adhikari B. Preparation of starch-based nanoparticles through high-pressure homogenization and miniemulsion cross-linking: Influence of various process

parameters on particle size and stability. *Carbohydr Polym*. 2011;83(4):1604-1610. doi:10.1016/j.carbpol.2010.10.011.

31. Valodkar M, Thakore S. Isocyanate crosslinked reactive starch nanoparticles for thermo-responsive conducting applications. *Carbohydr Res*. 2010;345(16):2354-2360. doi:10.1016/j.carres.2010.08.008.

32. Azizi Samir MAS, Alloin F, Dufresne A. Review of Recent Research into Cellulosic Whiskers, Their Properties and Their Application in Nanocomposite Field. *Biomacromolecules*. 2005;6(2):612-626. doi:10.1021/bm0493685.

33. Siqueira G, Bras J, Dufresne A. Cellulose Whiskers versus Microfibrils: Influence of the Nature of the Nanoparticle and its Surface Functionalization on the Thermal and Mechanical Properties of Nanocomposites. *Biomacromolecules*. 2009;10(2):425-432. doi:10.1021/bm801193d.

34. Rahman MS. *Food Properties Handbook, Second Edition*. CRC Press; 2009.

35. Atwell WA (Pillsbury R and DL, Hood LF, Lineback DR, Varriano-Marston E, Zobel HF. The terminology and methodology associated with basic starch phenomena. *Cereal Foods World USA*. 1988. http://agris.fao.org/agris-search/search.do?recordID=US8933107. Accessed January 30, 2017.

36. Olkku J, Rha C. Gelatinisation of starch and wheat flour starch—A review. *Food Chem*. 1978;3(4):293-317. doi:10.1016/0308-8146(78)90037-7.

37. Park H-M, Li X, Jin C-Z, Park C-Y, Cho W-J, Ha C-S. Preparation and Properties of Biodegradable Thermoplastic Starch/Clay Hybrids. *Macromol Mater Eng*. 2002;287(8):553-558. doi:10.1002/1439-2054(20020801)287:8<553::AID-MAME553>3.0.CO;2-3.

38. Charles AL, Kao H-M, Huang T-C. Physical investigations of surface membrane–water relationship of intact and gelatinized wheat–starch systems. *Carbohydr Res*. 2003;338(22):2403-2408. doi:10.1016/j.carres.2003.08.002.

39. Yoon S-Y, Deng Y. Clay–starch composites and their application in papermaking. *J Appl Polym Sci*. 2006;100(2):1032-1038. doi:10.1002/app.23007.

40. Avella M, De Vlieger JJ, Errico ME, Fischer S, Vacca P, Volpe MG. Biodegradable starch/clay nanocomposite films for food packaging applications. *Food Chem*. 2005;93(3):467-474. doi:10.1016/j.foodchem.2004.10.024.

41. García MA, Martino MN, Zaritzky NE. Starch-based coatings: effect on refrigerated strawberry (Fragaria ananassa) quality. *J Sci Food Agric*. 1998;76(3):411-420. doi:10.1002/(SICI)1097-0010(199803)76:3<411::AID-JSFA965>3.0.CO;2-I.

42. Petersson M, Stading M. Water vapour permeability and mechanical properties of mixed starch-monoglyceride films and effect of film forming conditions. *Food Hydrocoll*. 2005;19(1):123-132. doi:10.1016/j.foodhyd.2004.04.021.

43. Likhitkar S, Bajpai AK. Magnetically controlled release of cisplatin from superparamagnetic starch nanoparticles. *Carbohydr Polym*. 2012;87(1):300-308. doi:10.1016/j.carbpol.2011.07.053.

44. Thakur VK, Thakur MK. *Eco-Friendly Polymer Nanocomposites: Processing and Properties*. Springer; 2015.

45. Gonçalves PM, Noreña CPZ, da Silveira NP, Brandelli A. Characterization of starch nanoparticles obtained from Araucaria angustifolia seeds by acid hydrolysis and ultrasound. *LWT - Food Sci Technol*. 2014;58(1):21-27. doi:10.1016/j.lwt.2014.03.015.

46. Mueller S, Llewellin EW, Mader HM. The rheology of suspensions of solid particles. *Proc R Soc Lond Math Phys Eng Sci*. 2010;466(2116):1201-1228. doi:10.1098/rspa.2009.0445.

47. Mohsenipour AA. Turbulent Drag Reduction by Polymers, Surfactants and Their Mixtures in Pipeline Flow. 2011.

48. Saari H, Fuentes C, Sjöö M, Rayner M, Wahlgren M. Production of starch nanoparticles by dissolution and non-solvent precipitation for use in food-grade Pickering emulsions. *Carbohydr Polym*. 2017;157:558-566. doi:10.1016/j.carbpol.2016.10.003.

49. Steeneken PAM. Rheological properties of aqueous suspensions of swollen starch granules. *Carbohydr Polym*. 1989;11(1):23-42. doi:10.1016/0144-8617(89)90041-6.

50. Montgomery DC. *Design and Analysis of Experiments*. John Wiley & Sons; 2008. https://books.google.com/books?hl=en&lr=&id=kMMJAm5bD34C&oi=fnd&pg=PA1&dq=Design+and+Analysis+of+Experiments&ots=Kmr4Py5Mtw&sig=3ePYIZp3ZUQebmXskXd3eGW--H0. Accessed March 28, 2017.

51. Turbulent flow is slower than laminar flow | lorem ipsum. http://blog.nialbarker.com/252/slow_is_faster. Accessed April 18, 2017.

52. Metzner AB, Reed JC. Flow of non-newtonian fluids—correlation of the laminar, transition, and turbulent-flow regions. *AIChE J*. 1955;1(4):434-440. doi:10.1002/aic.690010409.

53. Gyr A, Bewersdorff H-W. *Drag Reduction of Turbulent Flows by Additives*. Vol 32. Springer Science & Business Media; 2013. https://books.google.com/books?hl=en&lr=&id=X-T6CAAAQBAJ&oi=fnd&pg=PA1&dq=Drag+Reduction+of+Turbulent+Flow+by+Additivies&ots=DegmEHfwPJ&sig=XQtgOxiAMWSLslDbHHb4qDtEEeo. Accessed March 29, 2017.

54. Marousis S n., Saravacos G d. Density and Porosity in Drying Starch Materials. *J Food Sci*. 1990;55(5):1367-1372. doi:10.1111/j.1365-2621.1990.tb03939.x.

Appendix A

Physical and Chemical Properties of Materials Used in This Thesis

1. Microbiocide

THOR

ACTICIDE® GA

Precautionary Statements:
Hazards to Humans and Domestic Animals

DANGER

CORROSIVE. CAUSES EYE DAMAGE AND SKIN BURNS. MAY CAUSE ALLERGIC SKIN REACTION. MAY BE HARMFUL IF INHALED OR ABSORBED THROUGH THE SKIN. DO NOT GET IN EYES, ON SKIN, ON CLOTHING. WEAR GOGGLES OR FACE SHIELD WHEN HANDLING. HARMFUL IF SWALLOWED. AVOID BREATHING VAPOR OR SPRAY MIST. AVOID CONTAMINATION OF FOOD. WASH THOROUGHLY WITH SOAP AND WATER AFTER HANDLING. REMOVE CONTAMINATED CLOTHING, AND WASH CLOTHING BEFORE REUSE.

Active Ingredients:
2-Bromo-2-nitropropane-1, 3-diol.....5.20%
5-Chloro-2-methyl-4-isothiazolin-3-one.....0.85%
2-Methyl-4-isothiazolin-3-one.....0.28%
Inert Ingredients:.....93.67%
Total:.....100.0%

KEEP OUT OF REACH OF CHILDREN

DANGER

See Side panel for additional precautionary statements

FIRST AID

IF SWALLOWED:
- Call a poison control center or doctor immediately for treatment advice.
- Have person sip a glass of water if able to swallow.
- Do not induce vomiting unless told to do so by a poison control center or doctor.
- Do not give anything by mouth to an unconscious person.

IF ON SKIN OR CLOTHING:
- Take off contaminated clothing.
- Rinse skin immediately with plenty of water for 15-20 minutes.
- Call a poison control center or doctor for treatment advice.

IF IN EYES:
- Hold eye open and rinse slowly and gently with water for 15-20 minutes.
- Remove contact lenses, if present, after the first 5 minutes, then continue rinsing eye.
- Call a poison control center or doctor for treatment advice.

IF INHALED:
- Move person to fresh air.
- If person is not breathing, call 911 or an ambulance, then give artificial respiration, preferably mouth-to- mouth, if possible.
- Call a poison control center or doctor for further treatment advice.

HOT LINE NUMBER: Have the product container or label with you when calling a poison control center or doctor, or going for treatment. You may also contact 1-800-424-9300 for emergency medical treatment information.

NOTE TO PHYSICIAN: Probable mucosal damage may contraindicate the use of gastric lavage. Measures against circulatory shock, respiratory depression and convulsions may be needed.

For Transportation / Spills Emergency
call Chemtrec at 1-800-424-9300

DIRECTIONS FOR USE
It is a violation of Federal Law to use this product in a manner inconsistent with its labeling.
Industrial microbiocide for use in adhesives, tackifiers, paints, coatings, building materials, polymer latices, printing inks, *metal working, *metal cleaning fluids, *fuels/oil/storage tank bottom water/crude, dispersions/emulsions/solutions/suspensions, aqueous compositions, *pulp and paper mills, * Industrial Water Systems, and other cleaners including liquid soaps, cleaners, detergents, carpet shampoos for industrial and household uses and in polishes and waxes. READ AND FOLLOW THE DIRECTIONS FOR USE ON THE ACCOMPANYING INFORMATION SHEET.
*** Not approved for use in the State of California**

EPA Reg. No. 67071-18 EPA Est. No 67071-DEU-001

Manufactured By/For: Thor GmbH
U.S. Office: Thor Specialties, Inc.
50 Waterview Drive, Shelton, CT
06484 USA
Tel. (203) 516-6980

UN 3265, CORROSIVE LIQUID, ACIDIC, ORGANIC, N.O.S. [mixture containing 5-Chloro-2-methyl-4-isothiazolin-3-one and 2-Methyl-4-isothiazolin-3-one (3:1)]. 8, PG-II

ENVIRONMENTAL HAZARDS
This pesticide is toxic to fish and wildlife. Do not discharge effluent containing this product into lakes, streams, ponds, estuaries, oceans or other waters unless in accordance with the requirements of a National Pollutant Discharge Elimination System (NPDES) permit and the permitting authority has been notified in writing prior to discharge. Do not discharge effluent containing this product to sewer systems without previously notifying the treatment plant authority. For guidance contact your State Water Board or Regional Office of the EPA.

STORAGE AND DISPOSAL
PROHIBITIONS: This product (pH 3.5) is corrosive to mild steel. Do not store in unlined containers. Do not contaminate food or feed by storage, disposal or cleaning of equipment.
PESTICIDE DISPOSAL: Pesticide wastes are acutely hazardous. Improper disposal of excess pesticide or rinsate is a violation of Federal law. If these wastes cannot be disposed of by use according to label instructions, contact your State Pesticide or Environmental Control Agency or the Hazardous Waste representative at the nearest EPA Regional Office for guidance.
CONTAINER DISPOSAL: Non-refillable container. Do not reuse or refill this container. Triple rinse container promptly after emptying. Triple rinse as follows: [For containers < 5 gallons in size] – Empty the remaining contents into application equipment or a mix tank and drain for 10 seconds after the flow begins to drip. Fill the container ¼ full with water and recap. Shake for 10 seconds. Pour rinsate into application equipment or a mix tank or store rinsate for later use or disposal. Drain for 10 seconds after the flow begins to drip. Repeat this procedure two more times. [For containers > 5 gallons in size] - Empty the remaining contents into application equipment or a mix tank. Fill the container ¼ full with water. Replace and tighten closures. Tip container on its side and roll it back and forth, ensuring at least one complete revolution, for 30 seconds. Stand the container on its end and tip it back and forth several times. Turn the container on its other end and tip it back and forth several times. Empty the rinsate into application equipment or a mix tank or store rinsate for later use or disposal. Repeat this procedure two more times. Then offer for recycling if available or puncture and dispose of in a sanitary landfill, or by other procedures approved by state and local authorities. ***GENERAL: CONSULT FEDERAL, STATE OR LOCAL DISPOSAL AUTHORITIES FOR APPROVED ALTERNATIVE PROCEDURES.***

CONDITIONS OF SALE AND WARRANTY
Thor GmbH warrants that the product conforms to its chemical description and is reasonably fit for the purpose stated on the label only when used in accordance with label directions under normal conditions of use. THOR GMBH MAKES NO OTHER EXPRESS OR IMPLIED WARRANTIES EITHER OF MERCHANTABILITY OR FITNESS FOR A PARTICULAR USE. Handling, storage and use of the product by Buyer or User are beyond the control of Thor GmbH and Seller. Risk resulting from ineffectiveness or other undesired consequences shall be borne by Buyer or User. Seller's or Thor GmbH's liability, if any, based on failure to follow label directions will be assumed by the Buyer or User. IN NO CASE WILL THOR GMBH OR SELLER BE HELD LIABLE FOR CONSEQUENTIAL, SPECIAL OR INDIRECT DAMAGES RESULTING FROM THE HANDLING, STORAGE OR USE OF THIS PRODUCT.

Label# 018-1 V001 08/14/2013

Batch: | Mfg Date: | Net Contents (pounds):

Appendix B

Apparatus Specification

1. Thermo Scientific Orion 3-Star Plus Conductivity Meters

The Thermo Scientific Orion 3-Star Plus conductivity meters work for a variety of applications and liquid purities.

Product Specifications

Thermo Scientific
Orion 3-Star Plus
Conductivity Meters

Features and Benefits

- Simultaneous display of conductivity, resistivity, TDS or salinity and temperature measurements on the backlit LCD
- The Thermo Scientific Orion SMART STABILITY™ and SMART AVERAGING™ functions for automatically optimized accuracy, precision and response time
- Meet all U.S. Pharmacopeia (USP) requirements
- Accept cell constants from 0.001 to 199.9 cm^{-1}
- Compatible with 2-electrode and 4-electrode conductivity cells
- Temperature calibration capability
- Conductivity / TDS / salinity / resistivity calibration of up to 5 points
- Reading reference temperatures at 5 °C, 10 °C, 15 °C, 20 °C or 25 °C
- Storage of up to 10 individually password-protected methods for easy retrieval of operation procedures
- Datalog up to 1000 points with time and date stamp
- RS232 port for easy data downloading and software updates
- Benchtop units can control an autosampler and the 096010 stirrer probe (*each sold separately*)
- Benchtop units are splashproof with an IP54-rated housing and include a universal power supply
- Portable units are waterproof with an IP67-rated housing and run for over 2,000 hours on four AA batteries
- 3 year meter warranty

Part of Thermo Fisher Scientific

Thermo SCIENTIFIC

Thermo Scientific Orion 3-Star Plus Conductivity Meters

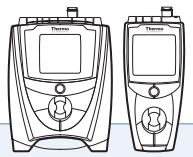

Conductivity	Range	0.000 to 3000 mS/cm, auto resolution with cell constant dependence
	Resolution	4 significant digits down to 0.001 µS/cm, cell constant dependent
	Relative Accuracy	0.5% ± 1 digit or 0.01 µS/cm, whichever is greater
	Cell Constants	0.001 to 199.9
Resistivity	Range	0.0001 to 100 Megohm
	Resolution	Automatic
	Relative Accuracy	0.5 % ± 1 digit
Salinity	Range	0.1 to 80.0 ppt NaCl equivalent, 0.1 to 42 ppt practical salinity
	Resolution	0.1
	Relative Accuracy	± 0.1 ± 1 digit
TDS	Range	0 to 19999
	Resolution	1 mg/L
	Relative Accuracy	± 0.5 % ± 1 digit
Temperature	Range	- 5 to 105 °C
	Resolution	0.1 up to 99.9 °C, 1.0 over 99.9 °C
	Relative Accuracy	± 0.1 °C

Meters Only

Cat. No.	Package
1114000	Includes benchtop meter, universal power and user guide
1214000	Includes portable meter, batteries and user guide

Benchtop Meter Kits

Cat. No. / *Application*	Sensor (s)	Accessories and Solutions
1114001 / *Fresh Water Wastewater*	• 013005MD DuraProbe conductivity cell, K = 0.475, 1 µS/cm to 200 mS/cm	• 1413 µS/cm conductivity standard (5 x 60 mL bottles) • Swing arm electrode stand
1114002 / *Ultra Pure Water*	• 013016MD Conductivity cell, K = 0.1, includes flow cell, 0.01 µS/cm to 300 µS/cm	• 100 µS/cm conductivity standard (5 x 60 mL bottles) • Swing arm electrode stand
1114003 / *Ultra Pure Water*	• 013016MD Conductivity cell, K = 0.1, includes flow cell, 0.01 µS/cm to 300 µS/cm	• 100 µS/cm conductivity standard (5 x 60 mL bottles) • Conductivity calibration resistor kit • Star Navigator 21 software with RS232 computer cable • Swing arm electrode stand

Portable Meter Kits

Cat. No. / *Application*	Sensor (s)	Accessories and Solutions
1214001 / *Fresh Water Wastewater*	• 013005MD DuraProbe conductivity cell, K = 0.475, 1 µS/cm to 200 mS/cm	• 1413 µS/cm conductivity standard (10 x 15 mL pouches) • Hard field case
1214002 / *Ultra Pure Water*	• 013016MD Conductivity cell, K = 0.1, includes flow cell, 0.01 µS/cm to 300 µS/cm	• 100 µS/cm conductivity standard (5 x 60 mL bottles)
1214003 / *Fresh Water Wastewater*	• 013610MD Conductivity cell, K = 0.55, includes 3 meter cable, 10 µS/cm to 200 mS/cm)	• 1413 µS/cm conductivity standard (10 x 15 mL pouches) • Hard field case
1214004 / *Ultra Pure Water*	• 013016MD Conductivity cell, K = 0.1, includes flow cell, 0.01 µS/cm to 300 µS/cm	• 100 µS/cm conductivity standard (5 x 60 mL bottles) • Hard field case
1214501 / *Fresh Water Wastewater*	• 013005MD DuraProbe conductivity cell, K = 0.475, 1 µS/cm to 200 mS/cm	• 1413 µS/cm conductivity standard (10 x 15 mL pouches) • Soft field case
1214503 / *Fresh Water Wastewater*	• 013610MD DuraProbe conductivity cell, K = 0.55, includes 3 meter cable, 10 µS/cm to 200 mS/cm	• 1413 µS/cm conductivity standard (10 x 15 mL pouches) • Soft field case
1214504 / *Ultra Pure Water*	• 013016MD Conductivity cell, K = 0.1, includes flow cell, 0.01 µS/cm to 300 µS/cm	• 100 µS/cm conductivity standard (5 x 60 mL bottles) • Soft field case
1214101 / *Fresh Water Wastewater*	• 013005MD DuraProbe conductivity cell, K = 0.475, 1 µS/cm to 200 mS/cm	—

S-3STARCD-E 0408 RevA

Environmental Instruments
Water Analysis Instruments

North America
166 Cummings Center
Beverly, MA 01915 USA
Toll Free: 1-800-225-1480
Tel: 1-978-232-6000
Dom. Fax: 1-978-232-6015
Int'l Fax: 978-232-6031

Europe
Denmark House, Angel Drove
Ely, Cambridgeshire
England, CB7 4ET
Tel: 44-1353-666111
Fax: 44-1353-666001

Asia Pacific
Blk 55, Ayer Rajah Crescent
#04-16/24, Singapore 139949
Tel: 65-6778-6876
Fax: 65-6773-0836

www.thermo.com/water

1 Introduction

Fann Model 35 viscometers are direct-reading instruments which are available in six- speed and twelve- speed designs for use on either 50 Hz or 60 Hz electrical power. The standard power source is 115 volts, but all models may be fitted with a transformer, making operation with 220/230 volts possible.

Fann Model 35 viscometers are used in research and production. These viscometers are recommended for evaluating the rheological properties of fluids, Newtonian and non-Newtonian. The design includes a R1 Rotor Sleeve, B1 Bob, F1 Torsion Spring, and a stainless steel sample cup for testing according to American Petroleum Institute Recommended Practice for Field Testing Water Based Drilling Fluids, API RP 13B-1/ISO 10414-1 Specification.

1.1 Background

Fann Model 35 viscometers are Couette rotational viscometers. In this viscometer, the test fluid is contained in the annular space (shear gap) between an outer cylinder and the bob (inner cylinder). Viscosity measurements are made when the outer cylinder, rotating at a known velocity, causes a viscous drag exerted by the fluid. This drag creates a torque on the bob, which is transmitted to a precision spring where its deflection is measured.

Viscosity measured by a Couette viscometer, such as the Model 35, is a measure of the shear stress caused by a given shear rate. This relationship is a linear function for Newtonian fluids (i.e., a plot of shear stress vs. shear rate is a straight line).

The instrument is designed so that the viscosity in centipoise (or millipascal second) of a Newtonian fluid is indicated on the dial with the standard rotor R1, bob B1, and torsion spring F1 operating at 300 rpm. Viscosities at other test speeds may be measured by using multipliers of the dial reading. A simple calculation that closely approximates the viscosity of a pseudo-plastic fluid, such as a drilling fluid is described in Section 7.

The shear rate may be changed by changing the rotor speed and rotor-bob combination. Various torsion springs are available and are easily interchanged in order to broaden shear stress ranges and allow viscosity measurements in a variety of fluids.

3 Features and Specifications

The Fann direct-indicating viscometers are equipped with the standard R1 rotor sleeve, B1 bob, F1 torsion spring, and a stainless steel sample cup. Other rotor-bob combinations and/or torsion springs can be substituted to extend the torque measuring range or increase the sensitivity of the torque measurement.

Each viscometer is supplied with a 115 volt motor. For operation on 230 volts, a step-down transformer is required.

The viscometers are available in six-speed and twelve-speed models.
See Table 3-1, Table 3-2, Table 3-3 and Table 3-4for specifications. Table 3-5 lists the recommended environmental conditions for use.

The photo in Figure 3-1 shows the viscometer and the detailed drawing in Figure 3-2 identifies the individual parts.

Figure 3-1 Model 35SA Viscometer

Table 3-1 Model 35 Viscometer Specifications

Model No.	Part No.	Electrical	No. of Speeds	Speeds
35A	207198	115V, 60 Hz, 90W	6	600, 300, 200, 100, 6, 3
35SA	207199	115V, 50 Hz, 90W	6	600, 300, 200, 100, 6, 3
35A/SR-12	207200	115V, 60 Hz, 90W	12	600, 300, 200, 180, 100, 90, 60, 30, 6, 3, 1.8, 0.9
35SA/SR-12	207201	115V, 50 Hz, 90W	12	600, 300, 200, 180, 100, 90, 60, 30, 6, 3, 1.8, 0.9

Table 3-2 Model 35 Viscometer Sizes

Model No.	Part No.	Dimensions (LxDxH)	Weight
35A	207198	15.2 x 6 x 10.5 in. 39 x 15 x 27 cm	15 lb 6.8 kg
35SA	207199	15.2 x 6 x 10.5 in. 39 x 15 x 27 cm	15 lb 6.8 kg
35A/SR-12	207200	15.2 x 6 x 10.5 in. 39 x 15 x 27 cm	15 lb 6.8 kg
35SA/SR-12	207201	15.2 x 6 x 10.5 in. 39 x 15 x 27 cm	15 lb 6.8 kg
35A w/ case	101671768	8 x 16 x 19 in. 20.3 x 40.6 x 48.3 cm	26 lb 11.8 kg
35SA w/ case	101671770	8 x 16 x 19 in. 20.3 x 40.6 x 48.3 cm	26 lb 11.8 kg

Table 3-3 Rotor and Bob Dimensions

Unit	Radius (cm)	Length (cm)	Cylinder Area (cm^2) x Radius (cm)
B1	1.7245	3.8	71.005
B2	1.2276	3.8	35.981
B3	0.86225	3.8	17.751
B4	0.86225	1.9	8.876
R1	1.8415	n/a	n/a
R2	1.7589	n/a	n/a
R3	2.5867	n/a	n/a

Table 3-4 Rotor-Bob Specifications

ROTOR-BOB	R1 B1	R2 B1	R3 B1	R1 B2	R1 B3	R1 B4
Rotor Radius, R_0 (cm)	1.8415	1.7588	2.5866	1.8415	1.8415	1.8415
Bob Radius, R_i (cm)	1.7245	1.7245	1.7245	1.2276	0.8622	0.8622
Bob Height, L (cm)	3.8	3.8	3.8	3.8	3.8	1.9
Shear Gap in Annulus (cm)	0.117	0.0343	0.8261	0.6139	0.9793	0.9793
Radii Ratio, R_i / R_0	0.9365	0.9805	0.667	0.666	0.468	0.468
Maximum Use Temperature (°C)	93	93	93	93	93	93
Minimum Use Temperature (°C)	0	0	0	0	0	0

Table 3-5 Range of Environmental Conditions

Maximum Altitude	6562 ft (2000 m)
Temperature Range	41°F to 104°F (5°C to 40°C)
Maximum Relative Humidity (RH)	80% RH at 87.8°F (31°C) or less 50% RH at 104°F (40°C)

5.1 Operating the Model 35A and 35SA

The Model 35A and 35SA viscometers operate at six speeds, ranging from 3 rpm to 600 rpm. To select the desired speed, set the speed switch (located on the right side of the base) to the high or low speed position as desired. Then turn the motor on and move the gear shift knob (located on the top of the instrument) to the position that corresponds to the desired speed.

Table 5-1 lists the positions for the viscometer switch and the gear knob combinations to obtain the desired speed. The viscometer gear shift knob may be engaged while the motor is running. Read the dial for shear stress values.

Table 5-1 Six-Speed Testing Combinations for Models 35A and 35SA

Speed RPM	Viscometer Switch	Gear Shift Knob
600	High	Down
300	Low	Down
200	High	Up
100	Low	Up
6	High	Center
3	Low	Center

5.2 Operating the Model 35A/SR-12 and 35SA/SR-12

The Model 35A/SR-12 and 35SA/SR-12 have twelve speeds for testing capabilities. To achieve this broader testing range from 0.9 rpm to 600 rpm, an additional gear box shift lever is used; it is located on the right side of the gear box. See Figure 5-1. Move this lever to the left or right as determined from Table 5-2.

Never change the gear box shift lever while the motor is running. Changing it while the motor is running will result in gear damage.

Only the viscometer gear shift knob (on top of the instrument) can be changed while the motor is running.

HAAKE

Sensor System MV

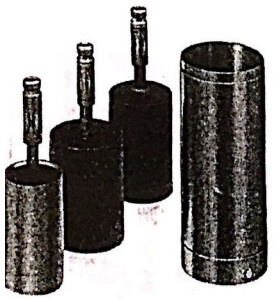

Application:

The MV is primarily used for viscosity measurements of medium viscous liquids such as heavy oils, paints, varnishes, resins, emulsions, etc. working in the medium shear rate range. Small yield points can be determined.

This coaxial cylinder sensor system consists of an MV cup used with three different rotors to provide different viscosity measuring ranges. MV I and MV II are both available in plastic (phenolic thermoset) and in stainless steel, 18/8. The plastic rotors are low weight and allow higher rates of rotor acceleration. They are mechanically and chemically safe for temperatures up to 100°C.

This sensor system requires the temperature vessel.

The rotors are positively mechanically centered. The top and the bottom surfaces of the rotors are recessed to minimize "end effects", i.e. their influence on torque. An air bubble is retained in the bottom recess, while the upper recess accomodates any excess sample.

The required amount of sample depends on the type of rotor used. For the purpose of reference there are two ring marks on the inside wall of the cup. The lower mark indicates the approximate sample volume required when the MV I and the MV II rotors are used in the cup MV. The upper ring mark is used for the MV III rotor.

Decreasing the temperature of a sample which just fills the annular gap between cup and rotor up to the upper rim of the rotor will cause the sample volume to shrink. This will lead to an only partly filled sensor system, to a reduced torque and to an erroneous viscosity value being below the true viscosity level.

When a sample must be measured at various temperatures, it is advisable to begin at the lowest temperature. When this is not possible, the sensor system MV should be overfilled to such an extent that the sample will be slightly above the rim of the rotor even at the lowest temperature. Rotor alternative: MV DIN (see 6.6).

During a test the liquid level of the sample must just overflow into the upper recess of the rotor. The liquid level must not surpass the upper rim of the rotor by more than 1 or 2 mm. Excess sample may be removed by sucking it back by means of a syringe.

Cleaning: To remove the bottom of the cup, first loosen the knurled screw and remove the cross-bar. (Order no. of sealing 807-0458)

HAAKE

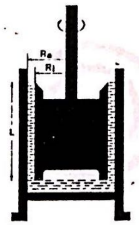

Sensor System	MV I	MV II	MV III
Inner Cylinder (rotor) radius R_i (mm)	20.04	18.4	15.2
height L (mm)	60	60	60
Outer Cylinder (cup) radius R_a (mm)	21	21	21
Radii Ratio R_a/R_i	1.05	1.14	1.38
Sample Volume V (cm^3)	40	55	70
Temperature: max. (°C)	100	100	100
min. (°C)	-30	-30	-30
Calculation Factors			
A (Pa/scale grad.)	3.22	3.76	5.44
M (min/s)	2.34	0.9	0.44
G (mPa·s/scale grad.·min)	1374	4171	12375

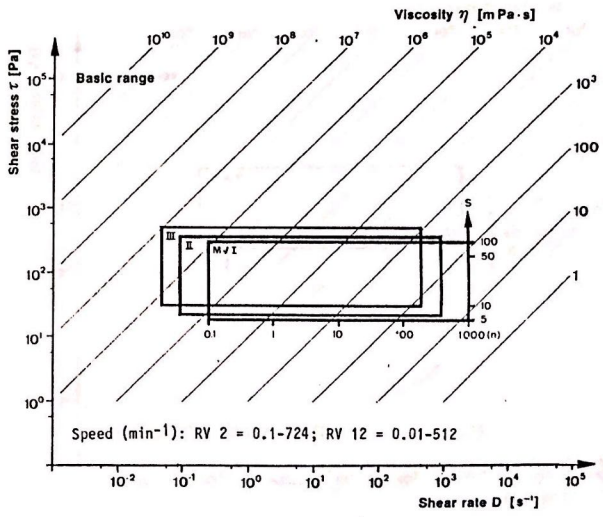

HAAKE

8.0 Evaluation

Principle: preset test speed "n" ⟶ read off torque "S".

The list of calculation factors (test certificate) shows the factors M, A and G. These factors are needed to calculate shear rate, shear stress and viscosity.

1) Shear rate D:

$D = M \cdot n \ (s^{-1})$

is calculated with "n"

M = "shear rate factor", depending on sensor system.

n = actual test speed

The actual test speed is calculated:

$$n = \frac{\text{set test speed}}{\text{reduction factor R}}$$

i.e. 64 min^{-1} on knob "R", position 10:

$$n = \frac{64}{10} = 6.4 \ min^{-1}$$

2) Shear stress τ:

$\tau = A \cdot S \ (Pa)$

is calculated with scale value "S".

A = "shear stress factor", depending on type of measuring drive unit and sensor system.

S = measuring value (scale grad)·sensitivity E.

The value to be obtained from this calculation is arrived at by multiplying the scale value by the set step "E", i.e. 57 scale grad on E = 0.3; S = 57·1/3 = 19 scale grad.

3) Viscosity η:

$\eta = \frac{G \cdot S}{n} (mPa \cdot s)$

Calculated with shear stress and shear rate.

G = "instrument factor", depending on the type of measuring drive unit and sensor system.

$G = 10^3 \cdot A/M \ (mPa \cdot s/\text{scale grad} \cdot min)$

Conversion of viscosity data from SI to CGS units:

Viscosity η : Pascal seconds (Pa·s); 1 Pa·s = 10 Poise; 1 mPa·s = 1 cp.
Shear stress τ : Pascal (Pa); 1 Pa = 10 dyne/cm^2
Shear rate D : Reciprocal second (1/s).

Thus the equation (1a) is changed to:

$$\eta = \frac{A \cdot S}{n} \ (mPa \cdot s) \qquad (1)$$

8.1 Equations for the evaluation

The designations used are:

M_d = torque at the rotor (Ncm)
L = height of the rotor (cm)
R_i = radius of the rotor (cm)
R_a = radius of the cup (cm)
n = speed of the rotor (min^{-1})
ω = opening angle of the cone (rad)
R_k = radius of the cone (cm)
f = shape factor
A = shear factor
a = torque-signal factor
M = shear rate factor
S = scale units on ordinate

Shear stress τ

The shear stress τ is linearly linked to the torque M_d:

$$\tau = f \cdot M_d \qquad (1)$$

The proportionality factor f recognizes the characteristic geometry of the rotor. One might call f the 'shape factor'. The shear stress τ can be calculated easily using the value 'S' measured in scale graduations:

$$\tau = A \cdot S$$

Combining (1) and (2) defines the shear stress factor A:

$$A = f \cdot a \quad \text{with } a = \text{torque/reading} = M_d/S \qquad (3)$$

The "a" value is a constant correlation factor to correlate the torque applied at the shaft of the measuring-drive-unit to the value "S" indicated. The value "a" depends on the constant of the torsional measuring spring and the electrical specifications of both the basic unit and the measuring-drive-unit. The true value of "a" is given in the list of calculation factors supplied with each measuring-drive-unit.

The shape factor "f" can be calculated for the range of sensor systems offered using the following equations:

Cylinder Sensor Systems

$$f = \frac{1}{2 \cdot \pi \cdot L \cdot R_i^2} \qquad (4)$$

It is common procedure to add to this value "f" a correction factor which originates from the unavoidable torque caused by the cylinder end faces (end-effects) and which is added to the real torque created by the mass sheared in the coaxial cylinder gap. Thus instead of the real rotor height L a corrected height L* takes place in equation (4).

$$L^* = L + \Delta L \qquad (5)$$

This value ΔL is defined by means of the procedure as stated in the German standard DIN 53 018, page 2.

Cone - and - Plate Sensor Systems

$$f = \frac{3}{2 \cdot \pi \cdot R_k^3} \qquad (6)$$

Shear rate D

The shear rate 'D' is linearly linked to speed 'n':

$$D = M \cdot n \qquad (7)$$

The proportionality factor M recognizes the characteristic geometry of the sensor system. It is defined as the shear rate per speed unit. The following equations define this M factor:

Cylinder Sensor Systems

$$M = \frac{\pi}{15} \cdot \frac{R_a^2}{R_a^2 - R_i^2} \qquad (8)$$

Cone-and-Plate Sensor Systems

$$M = \frac{\pi}{30 \cdot \alpha} \qquad (9)$$

Note: The new SI-unit of an angle is the "radiant" rad. This correlates to the normally used "degree angle" (°):

$$1° = \frac{\pi}{180}\ \text{rad} = 0.0174\ \text{rad}$$

Viscosity η:

The equation to calculate the viscosity of Newtonian liquids is:

$$\tau = \eta \cdot D \qquad (10)$$

When using the equations for τ (2) and D (7) this leads to:

$$A \cdot S = \eta \cdot M \cdot n$$

or with η:

$$\eta = \frac{A \cdot S}{M \cdot n} \qquad (11)$$

It is common practice to give viscosity in values of "milli Pascal seconds". Then (11) becomes:

$$\eta = 10^3 \cdot \frac{A \cdot S}{M \cdot n} \qquad (11a)$$

To simplify the equation a part of it is combined to a constant G being typical for each sensor system:

$$G = 10^3 \cdot \frac{A}{M} \qquad (12)$$

Thus the equation (11a) is changed to :

$$\eta = \frac{G \cdot S}{n}\ (\text{mPa} \cdot \text{s}) \qquad (13)$$

HAAKE

8.2 Determination of instrument constants

Shear rate D , shear stress τ, and viscosity η, are computed from test results of 'n' and 'S' with the sensor factors 'M' (shear rate factor), 'A' (shear stress factor), and 'G' (viscosity factor). These factors are found in the list of calculation factors delivered with each instrument. They were established by means of an absolute test of 'weighing torques' or they are, as for instance 'M' and 'f', calculated by using the geometrical dimensions of the sensor system

Sensor system	f · 10-4 (cm-3)	M (min/s)
NV	36.3	5.41
MV I / T I	65.7	2.34
MV II / T II	76.8	0.90
MV III	111	0.44
MV I P	65.8	2.0
MV II P	76.8	0.88
MV SP	87.8	11 *
SV I	253	0.89
SV II	768	0.89
SV II P	768	0.78
SV II FL	572	----
SV SP	253	4.4
MV DIN	55.8	1.29
SV DIN	369.4	1.29
MV-E	61.43	1.29
SV-E	322.1	1.29
HS I	1172	40 *
HS II	1142	10 *
PK V, 1°	305.6	6 *
PK I, 1°	1740	6 *
PKII, 1°	4775	6 *
PK V, 0.5°	305.6	12 *
PK I, 0.5°	1740	12 *
PKII, 0.5°	4775	12 *
PK V, 0.3°	305.6	20 *
PK I, 0.3°	1740	20 *
PKII, 0.3°	4775	20 *

* the factors given are values for reference only; for exact values, see list of calculation factors.

In case that an instrument is expanded by further measuring-drive-units the relevant values A for the range of sensor systems must be calculated:

Example - you need 'A', 'M' for RV 12 with M 150 and MV I.

The value 'a' of the measuring-drive-unit M 150 is 0.0147 Ncm/scale grad.
" " " M 500 is 0.049 Ncm/scale grad.
" " " M 1500 is 0.147 Ncm/scale grad.

Calculation of shear stress factor 'A':

$A = f \cdot a = f(\text{MV I}) \cdot a(\text{M 150})$

$A = 65.7 \cdot 10^{-4}\ \text{cm}^3 \cdot 0.0147\ \text{Ncm/scale grad.}$ $A = 0.966 \cdot 10^{-4}\ \text{N/cm}^2 \cdot \text{scale gr}$

$A = 0.966\ (\text{Pa/scale grad.})$

Calculation of shear stress factor 'M':

Taken from the above table.

Calculation of viscosity factor '

$G = \frac{A}{M} \cdot 1000 = \frac{0.966}{2.34} \cdot 1000 = 413$

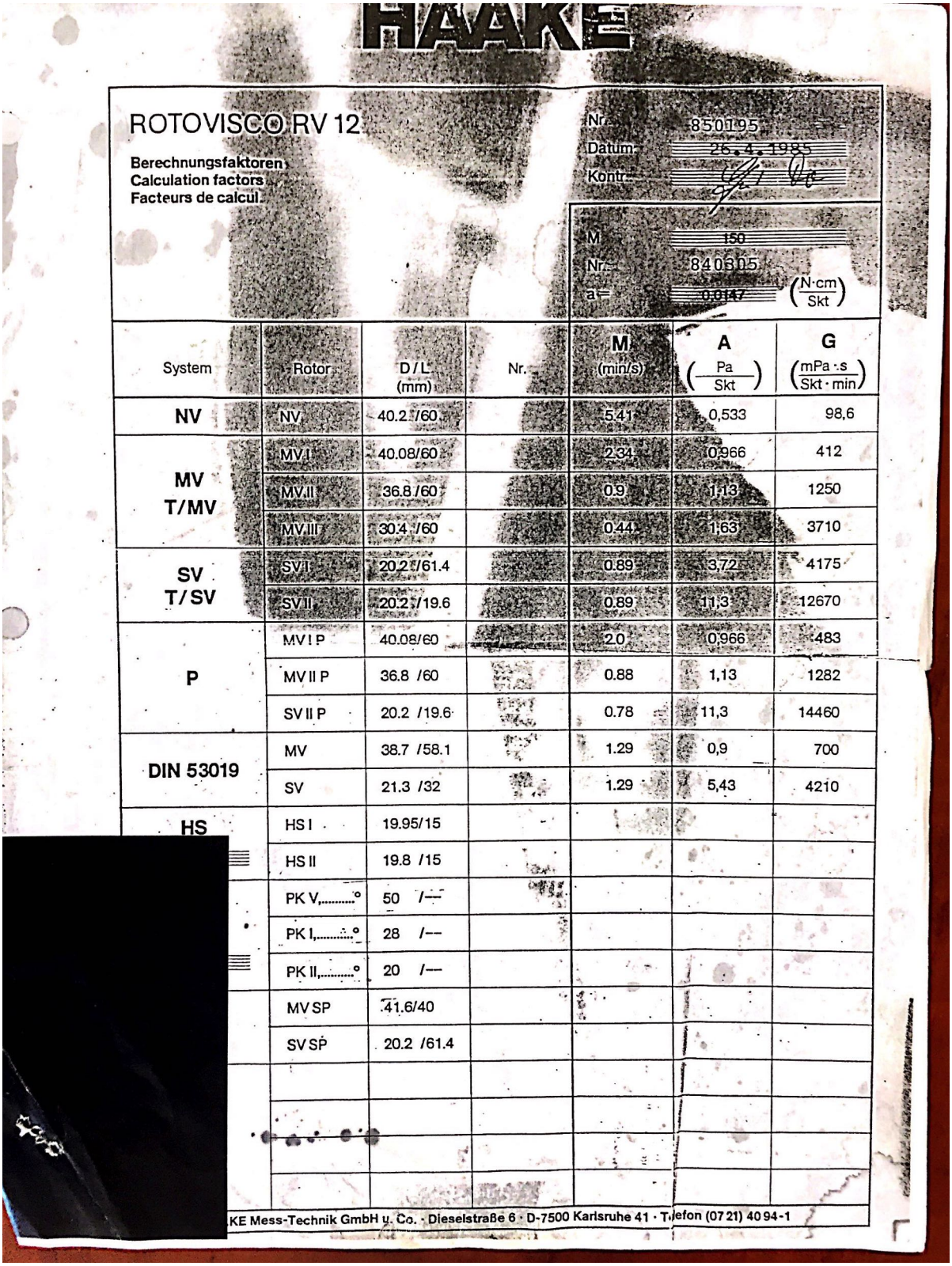

HAAKE

ROTOVISCO RV 12

Berechnungsfaktoren
Calculation factors
Facteurs de calcul

Nr. 850195
Datum 26.4.1985
Kontr.

M 150
Nr. 840305
a = 0.0147 $\left(\frac{N \cdot cm}{Skt}\right)$

System	Rotor	D/L (mm)	Nr.	M (min/s)	A $\left(\frac{Pa}{Skt}\right)$	G $\left(\frac{mPa \cdot s}{Skt \cdot min}\right)$
NV	NV	40.2 /60		5.41	0,533	98,6
MV T/MV	MV I	40.08/60		2.34	0,966	412
	MV II	36.8 /60		0.9	1,13	1250
	MV III	30.4 /60		0.44	1,63	3710
SV T/SV	SV I	20.2 /61.4		0.89	3,72	4175
	SV II	20.2 /19.6		0.89	11,3	12670
P	MV I P	40.08/60		2.0	0,966	483
	MV II P	36.8 /60		0.88	1,13	1282
	SV II P	20.2 /19.6		0.78	11,3	14460
DIN 53019	MV	38.7 /58.1		1.29	0,9	700
	SV	21.3 /32		1.29	5,43	4210
HS	HS I	19.95/15				
	HS II	19.8 /15				
	PK V,.....°	50 /—				
	PK I,.....°	28 /—				
	PK II,.....°	20 /—				
	MV SP	41.6/40				
	SV SP	20.2 /61.4				

KE Mess-Technik GmbH u. Co. · Dieselstraße 6 · D-7500 Karlsruhe 41 · Telefon (07 21) 40 94-1

4. CSC Precision and Interfacial DuNouy Tensiometers

A	Knurled Knob	J	Wire Retaining Screw
B	Sample Table Adjustment Screw	K	Rear Clamp Spring Support
C	Dial Clamp	L	Base Leveling Screw
D	Adjustable Stops	M	Torsion Arm
F	Fine Adjustment Screw	R	Cap
G	Adjustment Nut	S	Dial
H	Hook	T	Sample Table
I	Index	V	Vernier
		Y	Torsion Wire Cover

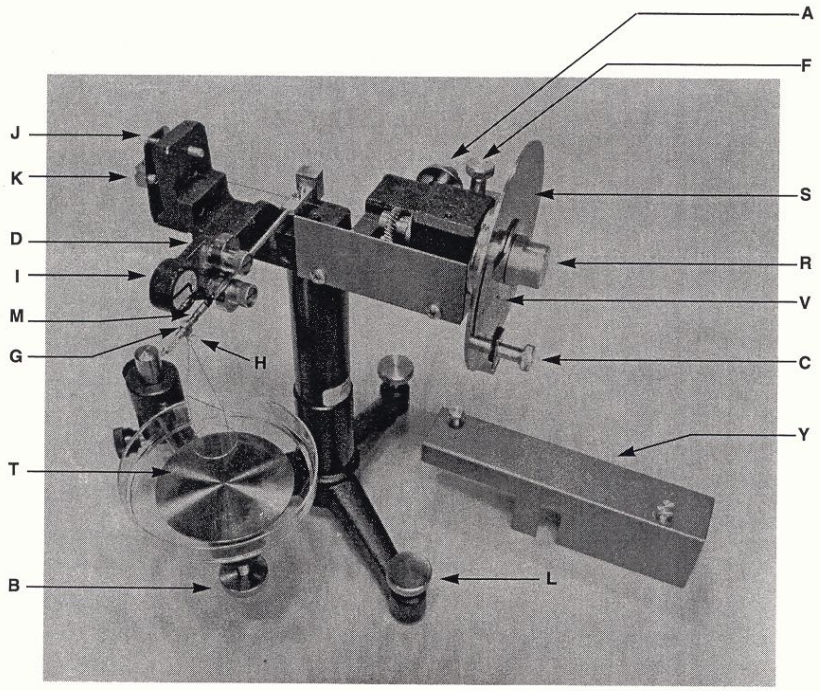

FIG. 1 - TENSIOMETER NO. 70535

-2-

A	Knurled Knob	L	Base Leveling Screw
B	Sample Table Adjustment Screw	M	Torsion Arm
C	Dial Clamp	N	Knurled Release
D	Adjustable Stops	P	Vertical Arm
E	Counter Weight	R	Cap
F	Fine Adjustment Screw	S	Dial
G	Adjustment Nuts	T	Sample Table
I	Index	V	Vernier
J	Wire Retaining Screw	X	Clamping Jaws
K	Rear Clamp Spring Support	Y	Torsion Wire Cover

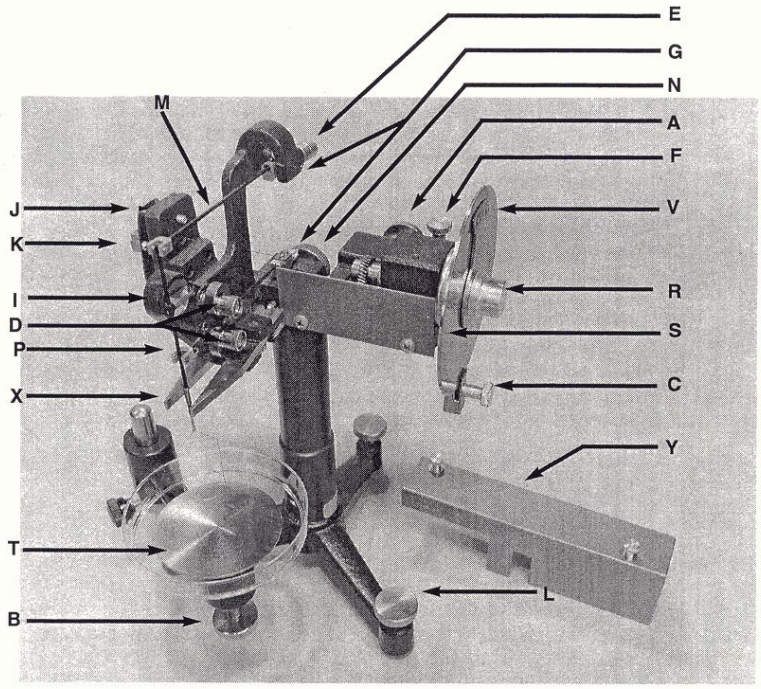

FIG. 2 - TENSIOMETER NO. 70545

dish, keeping the index of the lever arm at zero. The reading when the film at the interface breaks is the apparent interfacial tension p.

To make an interfacial measurement between water and a liquid denser than water, and instrument is required that will exert a downward force on the ring. CSC No. 70545 Tensiometer meets this requirement.

The measuring procedure is as follows: Pour the liquid of greater density in the vessel to a depth of 10 mm or more, then pour water to a depth of 5mm on the surface of the denser liquid. Raise the vessel until the ring is immersed in the water and is in the interface of the liquids with the lever arm index at zero. Increase the torsion on the wire to force the ring downward and, simultaneously raise the vessel, keeping the lever arm index at zero. The scale reading when the film breaks is the apparent interfacial tension.

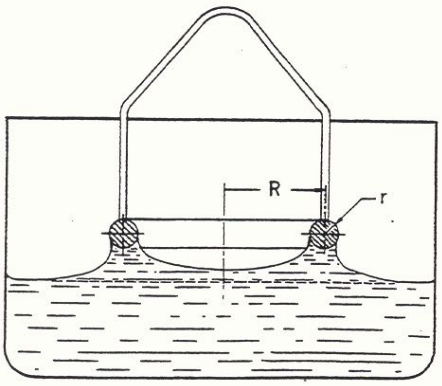

FIG. 3 - DISTENTION OF SURFACE FILM DURING SURFACE TENSION MEASUREMENT

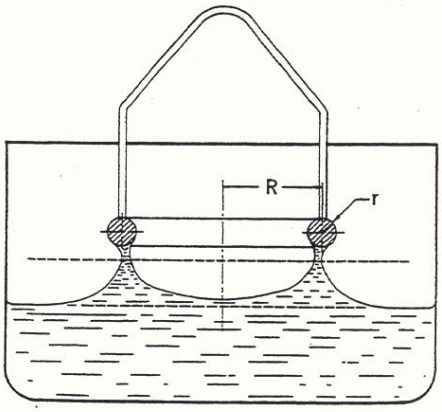

FIG. 4 - CONDITION OF SURFACE FILM AT BREAKING POINT

This tensiometers operate with a precision of ± 0.05 dynes/cm.

Zetasizer Nano range options

The Zetasizer Nano series of particle analysers consists of a range of different instrument models fitted with a choice of 'red' or 'green' lasers. The models and their measurement specifications are described in the table below, with instrument options following.

Zetasizer Nano	Size range maximum (diameter)	Size range for Zeta potential (diameter)	Molecular weight range (Daltons)	Accessory option (see below)
S	0.3nm to 10µm	–	342Da to $2x10^7$Da	ⒶⒹ ⒺⒻ
Z	–	3.8nm to 100µm	–	ⒶⒷⒸ ⒹⒺⒼ
ZS	0.3nm to 10µm	3.8nm to 100µm	342Da to $2x10^7$Da	ⒶⒷⒸⒹ ⒺⒻⒼ
S90	0.3nm to 5µm	–	342Da to $2x10^7$Da	ⒶⒹ ⒺⒻ*
ZS90	0.3nm to 5µm	3.8nm to 100µm	342Da to $2x10^7$Da	ⒶⒷⒸⒹ ⒺⒻ*
Nano ZSP	0.3nm to 10µm	3.8nm to 100µm	342Da to $2x10^7$Da	ⒶⒷⒸⒹ ⒼⒽ (Ⓕincluded as standard)

* Compatible but not recommended because of low sensitivity.

Ⓐ Narrow band filter	Ⓔ High temperature
Ⓑ Universal 'Dip' cell	Ⓕ Flow-mode option
Ⓒ High concentration cell	Ⓖ Microrheology
Ⓓ MPT-2 Titrator and Vacuum degasser	Ⓗ Protein mobility

For complete measurement specifications refer to the Basic Guide.

Laser type

The laser fitted is identified by the colour on the oval badge on the cover.

- Instruments with a black and **red** badge fitted to the instrument cover either have a 4mW 632.8nm 'red' laser or a 10mW 632.8nm 'red' laser (Nano ZSP only) fitted.
- Instruments with a Black and **green** badge have a 532nm 'green' laser fitted.

Appendix C
Raw Data Processing

1. Pipeline flow loop

As described at experiment method part, the voltage of different signal was directly measured, then using relative transformation function to get the desired result we need, such as flow rate and pressure drop. The whole calculation process will be demonstrated by the raw data of 0.1 wt% starch dispersion in the 1 inch pipe as follows.

Channel 1 / V	Channel 2 / V	Channel 3 / V	Pressure Drop / psi	Flow Rate (kg/s)
1.37	2.058		0.1492818	0.531696
1.472	2.642		0.2205882	0.6847776
1.55	3.178		0.2860338	0.80184
1.637	3.848		0.3678408	0.9324096
1.743	4.764		0.4796844	1.0914944
1.824	5.243	1.455	0.5482355	1.2130592
1.919		1.559	0.6790779	1.3556352
2.012		1.66	0.806146	1.4952096
2.106		1.775	0.9508275	1.6362848
2.207		1.907	1.1168967	1.7878656
2.375		2.153	1.4263893	2.04
2.58		2.473	1.8289813	2.347664
2.732		2.743	2.1686683	2.5757856
2.926		3.12	2.642972	2.8669408
3.116		3.51	3.133631	3.1520928
3.301		3.906	3.6318386	3.4297408
3.472		4.325	4.1589825	3.6863776
3.535		4.467	4.3376327	3.780928

The channel 1 represents the measuring voltage of flow rate, the channel 2 represents the measuring voltage of transducer at 0-0.5 psi and the channel 3 represents the measuring voltage of transducer at 0-5 psi.

For channel 1, we use this relationship to calculate the flow rate as “Flow Rate (kg/s)” column showed:

$$y = 1.5008\,x - 1.5244$$

For channel 2, we use this regression model to calculate the pressure drop:

$$y = 0.1221\,x - 0.1020$$

For channel 3, similarly we use this regression model to calculate the pressure drop:

$$y = 1.2581\,x - 1.2823$$

Then we calculate the Re and friction factor by flow rate and pressure drop as follows.

Flow Rate (kg/s)	Volume Rate (m^3/s)	Pressure Drop / psi	Pressure Drop / Pa	Re	f
0.531696	0.000532655	0.1492818	1029.261779	30695.49843	0.006376553
0.6847776	0.000686012	0.2205882	1520.9021	39533.09739	0.005680533
0.80184	0.000803286	0.2860338	1972.133628	46291.26129	0.005372146
0.9324096	0.000934091	0.3678408	2536.173037	53829.21334	0.005109193
1.0914944	0.001093463	0.4796844	3307.307514	63013.3848	0.004862039
1.2130592	0.001215247	0.5482355	3779.95071	70031.47809	0.004498928
1.3556352	0.00135808	0.6790779	4682.077302	78262.57515	0.004462105
1.4952096	0.001497906	0.806146	5558.18101	86320.38596	0.004354271
1.6362848	0.001639235	0.9508275	6555.724837	94464.8399	0.004288346
1.7878656	0.00179109	1.1168967	7700.731665	103215.7957	0.004219385
2.04	0.002043679	1.4263893	9834.608025	117771.8411	0.004138887
2.347664	0.002351897	1.8289813	12610.38215	135533.6821	0.004007221
2.5757856	0.00258043	2.1686683	14952.44157	148703.4374	0.003947113
2.8669408	0.002872111	2.642972	18222.65046	165512.204	0.003882943
3.1520928	0.003157777	3.133631	21605.62518	181974.3982	0.003808516
3.4297408	0.003435925	3.6318386	25040.64566	198003.3767	0.003728291
3.6863776	0.003693025	4.1589825	28675.17491	212819.3514	0.003695671
3.780928	0.003787746	4.3376327	29906.92468	218277.8684	0.003664054

2. Rheology

The rheology data were mainly measured by HAAKE viscometer Rotovisco® RV 12 with system MV I. According to the manual of this equipment, there are three factors for calculating the viscosity, shear rate and shear stress as follows:

M(Min/s)	A (Pa/Scale Grad)	G (mPa*s/Scale grad*min)
2.34	0.966	412

$$Viscosity = \frac{G * S}{n}$$

$$Shear\ rate = M * n$$

$$Shear\ stress = A * S$$

where n is set by the knobs of the equipment and S is the reading data.

The example data is the result of 10 wt% measured on July 7th:

		S					
n	Torque range	min	max	mean	Shear stress	Shear rate	Viscosity
25.6	3	2.9	3.1	1	0.966	59.904	16.09375
32	3	2.3	2.8	0.85	0.8211	74.88	10.94375
51.2	3	4.1	4.3	1.4	1.3524	119.808	11.265625
64	3	4.1	4.6	1.45	1.4007	149.76	9.334375
128	3	7.7	8.4	2.683333333	2.5921	299.52	8.636979167
256	3	15.3	15.7	5.166666667	4.991	599.04	8.315104167
512	1	22.5	23.3	22.9	22.1214	1198.08	18.42734375

Because the reading S is not stable at one point, a range reading of S is reasonable. The torque range just amplify the reading by 3, which makes the results more sensitive and accurate. Then we apply the above equations to calculate the shear stress, shear rate and viscosity.

3. Mass fraction transform to volume fraction

Based on previous published literature[54], the density of starch nanoparticles is around 1.5 g/cm³. And the relationship between mass fraction and volume fraction follows:

$$Volume\ fraction = \frac{Mass\ fraction * Density\ of\ suspension}{Density\ of\ starch\ nanoparticles}$$

That is:

$$Volume\ fraction = \frac{Mass\ fraction * Density\ of\ suspension}{1.5}$$

Mass fraction	Volume fraction	Density of suspension (g/cm³)
0.35	0.2677	1.1474
0.34	0.2584	1.1399
0.32	0.2414	1.1316
0.31	0.2333	1.129
0.3	0.2242	1.121
0.2875	0.2138	1.1156
0.275	0.2026	1.105
0.25	0.1832	1.099
0.2375	0.1731	1.093
0.225	0.1632	1.088
0.2	0.1436	1.077
0.175	0.1244	1.066
0.15	0.1055	1.055
0.125	0.0870	1.044
0.1	0.0688	1.032
0.0854	0.0581	1.02
0.08	0.0548	1.028
0.07	0.0478	1.0234
0.06	0.0408	1.0202
0.05	0.0339	1.0169
0.04	0.0270	1.0127
0.03	0.0202	1.0092
0.02	0.0134	1.0044
0.01	0.0067	1.0015

4. Density of starch nanoparticles dispersion at different mass fraction

Date	Concentration	Volume / ml	Mass / g			Mean / g	Density / (g/cm^3)
2016-08-10	36.00%	50	57.38	57.37	57.34	57.36	1.147
2016-08-08	35.00%	50	57.34	57.32	57.37	57.34	1.147
2016-08-10	35.00%	50	57.38	57.37	57.34	57.36	1.147
2016-08-10	35.00%	50	57.36	57.45	57.41	57.41	1.148
2016-08-04	34.00%	50	56.96	56.95	57.08	57.00	1.140
2016-08-08	34.00%	50	57.23	57.19	57.22	57.21	1.144
2016-08-09	34.00%	50	57.1	57.11	57.18	57.13	1.143
2016-08-04	32.00%	50	56.6	56.77	56.69	56.69	1.134

2016-07-29	32.00%	50	56.42	56.43	56.46	56.44	1.129
2016-08-08	32.00%	50	56.68	56.79	56.67	56.71	1.134
2016-08-15	32.00%	50	56.46	56.49	56.5	56.48	1.130
2016-08-08	31.00%	50	56.42	56.54	56.45	56.47	1.129
2016-08-10	31.00%	50	56.38	56.45	56.42	56.42	1.128
2016-08-10	31.00%	50	56.4	56.46	56.53	56.46	1.129
2016-07-27	30.00%	50	56.09	56.04	56.14	56.09	1.122
2016-07-20	30.00%	50	55.98	56.01	56.02	56.00	1.120
2016-07-27	28.75%	50	55.78	55.85	55.67	55.77	1.115
2016-07-20	28.75%	50	55.77	55.77	55.85	55.80	1.116
2016-07-18	27.50%	50	55.05	54.92	54.78	54.92	1.098
2016-07-13	27.50%	50	55.49	55.54	55.61	55.55	1.111
2016-07-20	25.00%	50	54.91	54.93	54.98	54.94	1.099
2016-07-20	23.75%	50	54.64	54.64	54.72	54.67	1.093
2016-07-18	22.50%	50	54.45	54.44	54.51	54.47	1.089
2016-07-13	22.50%	50	54.26	54.33	54.37	54.32	1.086
2016-07-18	17.50%	50	53.27	53.36	53.28	53.30	1.066
2016-07-13	17.50%	50	53.23	53.33	53.2	53.25	1.065
2016-07-18	12.50%	50	52.15	52.32	52.18	52.22	1.044
2016-07-13	12.50%	50	52.14	52.15	52.18	52.16	1.043
2016-08-03	8.00%	50	51.37	51.41	51.42	51.40	1.028
2016-08-03	7.00%	50	51.14	51.18	51.19	51.17	1.023
2016-08-03	6.00%	50	51	51	51.03	51.01	1.020
2016-08-03	5.00%	50	50.86	50.83	50.84	50.84	1.017
2016-08-04	5.00%	50	50.79	50.77	50.87	50.81	1.016
2016-08-03	4.00%	50	50.64	50.64	50.62	50.63	1.013
2016-08-03	3.00%	50	50.44	50.45	50.49	50.46	1.009
2016-08-03	2.00%	50	50.2	50.24	50.22	50.22	1.004
2016-08-03	1.00%	50	50.07	50.08	50.08	50.08	1.002